Purdue University
Purdue e-Pubs

Open Access Theses

Theses and Dissertations

Fall 2014

Dropwise Condensation Dynamics in Humid Air

Julian Eduardo Castillo Chaco
Purdue University

Follow this and additional works at: https://docs.lib.purdue.edu/open_access_theses

Part of the Mechanical Engineering Commons, and the Plasma and Beam Physics Commons

Recommended Citation

Castillo Chaco, Julian Eduardo, "Dropwise Condensation Dynamics in Humid Air" (2014). *Open Access Theses*. 306.
https://docs.lib.purdue.edu/open_access_theses/306

This document has been made available through Purdue e-Pubs, a service of the Purdue University Libraries. Please contact epubs@purdue.edu for additional information.

Graduate School Form 30
(Updated 11/20/2014)

PURDUE UNIVERSITY
GRADUATE SCHOOL
Thesis/Dissertation Acceptance

This is to certify that the thesis/dissertation prepared

By Julian Eduardo Castillo

Entitled
Dropwise Condensation Dynamics in Humid Air

For the degree of Master of Science in Mechanical Engineering

Is approved by the final examining committee:

Suresh V. Garimella

Justin A. Weibel

Liang Pan

To the best of my knowledge and as understood by the student in the Thesis/Dissertation Agreement, Publication Delay, and Certification/Disclaimer (Graduate School Form 32), this thesis/dissertation adheres to the provisions of Purdue University's "Policy on Integrity in Research" and the use of copyrighted material.

Approved by Major Professor(s): Suresh V. Garimella

Approved by: Ganesh Subbarayan 11/04/2014

Head of the Department Graduate Program Date

DROPWISE CONDENSATION DYNAMICS IN HUMID AIR

A Thesis

Submitted to the Faculty

of

Purdue University

by

Julian Eduardo Castillo Chacon

In Partial Fulfillment of the

Requirements for the Degree

of

Master of Science in Mechanical Engineering

December 2014

Purdue University

West Lafayette, Indiana

Para mi madre y padre

A ustedes debo cuanto he tenido

ACKNOWLEDGEMENTS

I would like to thank to my mentors, Professor Suresh V. Garimella and Professor Justin A. Weibel, for their invaluable guidance and support through the course of the last two years, and for influencing my academic career and personal life positively. I also give thanks to Dr. Deanne Kemeny for her care and help. I am also grateful to my thesis review committee, Professor Liang Pan, for his helpful guidance that has led to success of this work.

I thank my parents, sisters, and grandmother for their everlasting care, love, and sacrifices. I also give thanks to all my collages in the Cooling Technologies Research Center (CTRC) for their help with the work and unconditional friendship: Susmita Dash, Carolina Mira, Kevin Drummond, Aditya Chandramohan, Ravi Patel, Matt Rau, Steve Taylor, Suchismita Sarangi, Pierre Valiorgue, Richard Simmons, Niki Ritchey, Simone Mancin, Xuemei Chen, Dongseob Kim, and Yashwanth Yadavalli. Likewise, I thank Mr. Steve Titolo for manufacturing the experimental test facility.

I also acknowledge the financial support provided by the Cooling Technologies Research Center (CTRC), an NSF Industry/University Cooperative Research Center at Purdue University, the Colombian department for science, technology and innovation (Colciencias), the Colombia-Purdue Institute (CPI), the “Francisco José de Caldas”-

Fulbright Scholarship Program, and the Academic and Professional Programs for Americas (LASPAU).

TABLE OF CONTENTS

APPENDICES

LIST OF TABLES

Appendix Table Page

LIST OF FIGURES

Appendix Figures

NOMENCLATURE

k	thermal conductivity (W/mK)
R	single droplet radius (µm)
$<R>$	average radius (µm)
RH	relative humidity (%)
V	volume of condensate on the surface (ml)
t	time (min)
T	temperature (°C)

Greek

ε	surface coverage
μ	power-law exponent for droplet radius growth

Subscripts

sub	subcooling
ii	second regime of droplet growth
iii	third regime of droplet growth
A	first sub-regime within *ii*
B	second sub-regime within *ii*
1	regime ii_A to ii_B transition
2	regime *ii* to *iii* transition
3	end of regime *iii*

ABSTRACT

Castillo, Julian E. M.S.M.E., Purdue University, December 2014. Dropwise Condensation Dynamics in Humid Air. Major Professor: Suresh V. Garimella and Justin A. Weibel, School of Mechanical Engineering.

Dropwise condensation of atmospheric water vapor is important in multiple practical engineering applications. The roles of environmental factors and surface morphology/chemistry on the condensation dynamics need to be better understood to enable efficient water-harvesting, dehumidication, and other psychrometric processes. Systems and surfaces that promote faster condensation rates and self-shedding of condensate droplets could lead to improved mass transfer rates and higher water yields in harvesting applications. The thesis presents the design and construction of an experimental facility that allows visualization of the condensation process as a function of relative humidity. Dropwise condensation experiments are performed on a vertically oriented, hydrophobic surface at a controlled relative humidity and surface subcooling temperature. The distribution and growth of water droplets are monitored across the surface at different relative humidities (45%, 50%, 55%, and 70%) at a constant surface subcooling temperature of 15 °C below the ambient temperature. The droplet growth dynamics exhibits a strong dependency on relative humidity in the early stages during which there is a large population of small droplets on the surface and single droplet growth dominates over coalescence effects. At later stages, the dynamics of droplet growth is insensitive to relative humidity due to the dominance of coalescence effects. The overall volumetric rate of condensation on the surface is also assessed as a function of time and ambient relative humidity. Low relative humidity conditions not only slow the absolute rate of condensation, but also prolong an initial transient regime over which the condensation rate remains significantly below the steady-state value. The current state-of-the-art in dropwise condensation research indicates the need for systematic experimental investigations as a function of relative humidity. The improved understanding of the relative humidity effects on the growth of single and distributed droplets offered in this thesis can improve the prediction of heat and mass transfer during dropwise condensation of humid air under differing environmental conditions. This knowledge can be used to engineer condenser systems and surfaces that are adapted for local ambient relative humidity and temperature conditions.

CHAPTER 1. INTRODUCTION

1.1 Motivation

Condensation of atmospheric water vapor is exploited in water harvesting [1,2], dehumidification [3], distillation/desalination [4], building heating and cooling [5], and other engineered systems. Enhancement of the mass transfer rate during condensation and facilitation of liquid removal from the surface can reduce operational cost and improve efficiency in these applications.

In the presence of humid air, water condenses on a surface that has been cooled below the saturation temperature corresponding to the partial pressure of the vapor present in the air mixture (*i.e.*, the dew-point temperature). Depending on the wettability of the surface, the condensate may form a liquid film (wetting) or distinct droplets (non-wetting). Dropwise condensation is preferred over filmwise condensation due to the higher rates of heat and mass transfer that may be achieved [6]; however, condensate droplets must be promptly removed after nucleation on the surface in order to take advantage of the high rates of mass transfer and sustain the high rate of condensation. Surface functionalization and engineering has been investigated [7,8] to reduce the pinning forces between the droplets and the surface, and hence the departure size, compared to conventional smooth surfaces [9,10]. On the other hand, the rate of condensation is also governed by external atmospheric conditions (*viz.,* relative humidity, wind speed, and surface cooling). In order to predict and evaluate the performance of systems reliant on condensation, it is equally important to understand how these external conditions affect the dynamics of dropwise condensation.

1.2 Overview of Dropwise Condensation Dynamics

The dynamics of condensation of water vapor from air into liquid droplets on a surface has been extensively characterized [11-17]. Three stages of droplet growth may be identified [12,14-16]: (*i*) initially a uniform layer of small droplets grows only by direct condensation on the interfaces of the droplets; (*ii*) as the droplets grow, they coalesce and the distance between adjacent droplets increases with time; and (*iii*) small droplets appear in the exposed space between the droplets and the average surface coverage asymptotically increases to a constant value. Once the droplets reach a critical size, they slide off the surface and new droplets grow in the spaces that have been swept clear. A combination of experimental observations, scaling analyses, and numerical modeling of condensation on non-wetting surfaces [15] showed that during the second regime, the growth of single droplet radii can be described by the power law $R \sim t^{\mu}$, where $\mu = 1/3$. The average droplet radius followed $<R>\sim t^{\mu_{ii}}$ where μ_{ii} = 1 (under ideal conditions where the flux of water vapor molecules to the surface is uniform). Experimentally reported values for μ_{ii} are typically lower than unity due to the difference in boundary conditions from this idealized condition. Prior experimental investigations have only been performed at near 100% relative humidity, and the dependence of these reported rates of growth on relative humidity has not been experimentally investigated in the literature.

1.3 Objectives

The aim of the current study is to perform a systematic investigation of the dynamics of single and multiple droplet growth during dropwise condensation at controlled conditions not previously explored in the literature. Experiments are conducted in order to understand how the relative humidity affects the mechanisms that govern dropwise condensation dynamics, and to relate those effects to the overall mass transfer rate during the process.

1.4 Overview of the Document

This thesis is organized in four chapters as follows. Chapter 1 introduces the motivation for this study and provides perspectives on the potential utility of the current work. Chapter 2 provides a review of the pertinent literature on dropwise condensation. The effect of relative humidity on single droplet growth dynamics and the droplet distribution are presented in Chapter 3. Chapter 4 summarizes the conclusions and outlines suggestions for future work.

CHAPTER 2. LITERATURE REVIEW

The first report on dropwise condensation presented by Schmidt and Sellschopp [21] in 1930 recognized that dropwise condensation offers larger heat transfer coefficients than filmwise condensation. Additional reports on the methods to promote and sustain dropwise condensation were released in the 1970's [22-24]; research primarily focused on coating surfaces with low surface energy materials. During subsequent decades, additional advanced surface engineering techniques have been applied to further enhance the rates of heat and the mass transfer achieved during dropwise condensation by promoting early departure of droplets via gravitational forces or coalescence-induced jumping.

This chapter provides a review of the current state-of-the-art in dropwise condensation research in four sections: the first section reviews the parameters that influence heterogeneous nucleation of liquid from vapor, the second section reviews characteristics of single droplet growth, the third section reviews global dynamics of the condensation process, and the last section reviews factors that enhance heat and mass transfer during dropwise condensation.

2.1 Overview of Heterogeneous Nucleation

Classical nucleation theory predicts the dependency of nucleation on surface wettability, super saturation, and surface subcooling [25]. Heterogeneous nucleation of droplets will occur preferentially at defects present on a substrate [26] (*e.g.*, scratches, impurities, surface roughness, and chemical heterogeneities). The energy barrier required for droplet nucleation depends on the intrinsic wettability of the surface; as contact angle decreases, the energy barrier for nucleation decreases, which allows condensation to occur at temperature differentials much lower than required for homogeneous nucleation, and yields comparatively higher rates of nucleation [11,26].

Surface roughness has a strong effect on nucleation, and increases the nucleation site density [14,18,25]. Ucar and Erbil [60] reported condensation of moist air at a relative humidity of 63 % on polymer surfaces with different surfaces roughness. They showed that surface roughness and surface subcooling altered the initial droplet density. Leach *et al.* [19] observed condensation of an air-water vapor mixture on hydrophobic polymer films and silanized glass slides. Initial droplet densities varied from 10^4 to 10^6 drops/cm^2 as the temperature of the vapor-air mixture decreased from 97 °C to 30°C; they attributed this change to a reduction in the partial pressure of the vapor-air mixture. To date, there has been no comprehensive investigation of the effect that relative humidity has on dropwise condensation incipience or initial droplet density.

2.2 Single Droplet Growth Characteristics

Upon nucleation, liquid droplets are formed on the surface at the minimum nucleation radius ($R_{\min} \sim 10^{-3}$ µm for water); from this initial size, droplets grow by condensation directly on their liquid-vapor interface. Several studies on the dynamics of the drop growth showed that single droplet radius growth followed a power law of the form $R \sim t^{\mu}$, where the exponent μ is indicative of the dynamics of the growth. McCormick and.

Westwater [26] reported $\mu = 0.5$ for condensation of water vapor on copper and Ichikawa *et al.* [27] reported $\mu \approx 0.66-0.5$ for water condensation on silanized glass. Beysens and co-workers [11-15,28] reported $\mu \approx 0.33$ for the growth of water drops on a variety of different substrates when a constant volumetric flux of vapor was supplied to the surface. More recently, studies of condensation on superhydrophobic surfaces at enhanced spatial and temporal resolution, by using environmental electron scanning microscopy (ESEM) at low pressures, have shown similar dynamics of droplet growth. Miljkovic *et al.* [58], Rykaczewski [35], and Varanasi *et al.* [57] all reported a power-law exponent for growth of the individual droplets to be $\mu \approx 0.5$.

A power law with constant exponent fails to universally describe single droplet radius growth due to redistribution of vapor surrounding the droplets during condensation. When vapor primarily diffuses to the liquid-vapor interface, the rate of radius growth is independent of drop size; this is the case for large drops where the perimeter-to-area ratio is small. On the contrary, smaller droplets that have high perimeter-to-area ratios would grow primarily on the three-phase contact line of the droplet [30]. Viovy *et al.* [12] described droplet radius growth rates by including coefficients specific to each mode of condensation (interfacial or contact-line condensation), which lead to effective power-law exponents that depended both on droplet size and surface coverage. Leach *et al.* [19] reported single droplet radius growth rates (dR / dt) with a strong dependence on droplet size. Droplets with diameters smaller than ~50 µm grew predominantly by diffusion of water vapor from the bare spaces between the drops, while drops with diameter greater than ~50 µm grew by direct condensation from the vapor above to the liquid-gas interface of the droplet. Between these two limits, Leach and coworkers [19] described single droplet growth using power-law exponents varying between $0.5 < \mu < 1$. Sokuler *et al.* [31] reported variations in power-law radius growth exponents due to the presence of neighboring drops; alteration of the surrounding vapor distribution as a result of changes in the inter-droplet spacing lead to $\mu = 1/3$ for closely packed arrays of droplets and $\mu = 1/2$ for isolated droplets. Several additional factors such as time, surface geometry, and fluid properties seem to also affect the dynamics of the growth of a single drop, hence the spread in values reported in the literature.

2.3 Evolution of the Droplet Size Distribution

The cyclical distribution of droplet sizes present on the surface during dropwise condensation has been studied extensively. Since the pioneering work of Le Ferve and Rose [31], who first introduced the concept of droplet size distribution as a tool to assess rates of heat transfer during dropwise condensation, numerous models have been proposed to describe the droplet size distribution. A detailed review of extant models was prepared by Watanabe [33]. As highlighted in this review, one important characteristic of the evolution of droplet size distribution is that, under certain conditions (*e.g.*, low contact angle hysteresis, absence of nucleation of new droplets on bare surface, and homogenous surface wettability), there are consistent geometrical similarities in the distribution at multiple scales; thus, scaling laws are suitable for describing average droplet growth behavior.

Experimental observations by Beysens and Knobler [11] of condensation of saturated nitrogen on a vertically oriented hydrophobic surface showed that scale-invariant average droplet radius growth follows a power law given by $< R >\sim t^{\mu_{ii}}$, where μ_{ii} = 0.75±0.5 (approximately three time greater than μ for single droplet radius growth). This increment in the exponent for average radius growth is caused by coalescence of neighboring drops, which shifts the droplet size distribution to larger radii and widens the distribution range. Viovy *et al.* [12] introduced a theoretical model that describes growth with a power-law exponent of μ_{ii} = 1.0 (resulting from scaling single droplet growth where μ = 1/3). Briscoe and Galvin [30] reported on condensation of water on polyethylene films; they measured μ_{ii} = 0.67 when growth was limited by the rate at which the latent heat could be dissipated and μ_{ii} = 1.0 when the latent heat was easily dissipated.

2.4 Enhancing Dropwise Condensation

An important attribute of dropwise condensation is the critical size at which droplets can be removed from the surface (droplet size at which gravitational forces overcome capillary forces that adhere the droplet to the surface). Droplets sliding from the surface sweep clear additional droplets in their path, leading to a clean surface area where new, smaller droplets can nucleate. Also, during dropwise condensation, small drops ($R \sim$ 10 µm) transfer heat more efficiently than larger drops [8,22,58]; increasing the percentage of small droplets on the surface (by removing droplets at the smallest possible size) is hence highly desired. A common way to promote droplet removal is to passively take advantage of gravity by either tilting the surface at a small angle [36,37] or orienting it vertically [38]. Another method to enhance droplet mobility is using surface energy gradients [28,39]. Macner *et al.* [20] showed such surfaces shifted the droplet size distribution toward a population of smaller drops in comparison with uniform energy surfaces.

Several reports have proposed the use of superhydrophobic surfaces to promote condensation [34,47,53]. Dietz *et al*. [34] investigated the droplet departure frequency on superhydrophobic surfaces formed out of cupric hydroxide nanostructures; the surfaces shifted the drop size distribution to smaller radii by decreasing the critical droplet departure size. When a droplet is placed onto a structured surperhydrophobic surface, its contact area with the top-most surface roughness features is minimal (Cassie state). However, when a droplet is formed by condensation on the surface, nucleation of droplet within the roughness features limits mobility by pining the droplet to the surface [41,43]. In order to avoid these limitations, surfaces that promote condensate droplet formation in the Cassie state have been investigated [43,45].

Since Boreyko and Chen [7] first demonstrated that coalescence of micro-scale droplets on nanostructured superhydrophobic surfaces will release surface energy and cause the droplets to jump away from the surface against gravity, an increasing interest in this phenomenon has emerged; superhydrophobic nanostructured surfaces are now designed to promote droplet jumping induced removal [46,52], Miljkovic *et al.*[53] reported 30% improvements in condensation heat transfer coefficients using nanostructured CuO surfaces that promoted droplet jumping during condensation as compared to state-of-the-art dropwise condensation surfaces.

An alternative approach to promote dropwise condensation is to increase drop mobility by using textured surfaces impregnated with a lubricating liquid [55], which allow droplets to have extremely low contact angle hysteresis (~ 1°). Anand *et al.* [56] recently reported enhanced droplet departure on a surface with hierarchical micro-nanoscale texture impregnated with lubricant; condensate droplets as small as 100 µm became highly mobile.

CHAPTER 3. THE EFFECT OF RELATIVE HUMIDITY ON DROPWISE CONDENSATION DYNAMICS

This section presents a detailed description of the condensation facility and experimental procedure. Dropwise condensation experiments are performed at four relative humidities (RH = 45%, 50%, 55%, and 70%) and a constant surface subcooling temperature (ΔT_{sub} = 15 °C. The effect of surface subcooling on droplet growth at RH = 70% and ΔT_{sub} = 5 °C , 10 °C and 15 °C is included in Appendix C. The condensation dynamics (i.e., the droplet growth and distribution) are characterized as a function of relative humidity. The dependence of these dynamics on the relative humidity is then used to explain the trends in the rate of volume accumulation on the surface for a generation of condensate droplets.

3.1 Experimental Methods

3.1.1 Surface Preparation

The condensation experiments are performed on smooth silicon surfaces, coated with Teflon (AF 1600, Dupont) to render them hydrophobic. The silicon substrates were rinsed with isopropyl alcohol and ethanol for 5 min each, blown dry with nitrogen gas, and placed on a hot plate for 10 min at 90 °C. The wafers were then spin-coated with 2% mass fraction solution of Teflon in FC-77 at 4500 rpm and baked at 90°C for 40 min to eliminate the remaining solvent. This process yields a ~4.1 μm-thick hydrophobic film coating on the silicon surface.

3.1.2 Fluid Conditioning System

A schematic diagram of the experimental fluid conditioning system is shown in Figure 3.1.1. A list of all the components used and CAD drawings of the experimental facility are provided in Appendix A. The experimental facility has two separate flow circuits: Circuit A-B consists of a chiller (ThermoFlex, 900 W, Thermo Scientific) that recirculates cooled water through a cold plate (CP12, Lytron) attached to the test section. Circuit C-G adiabatically mixes dry nitrogen gas with nitrogen saturated with water vapor at controlled mass flow rates to achieve a desired relative humidity in the test section. Dry nitrogen entering (C) is regulated to 60 psi. Two downstream mass flow controllers (FMQ 5400, 0-2 SLM, Omega) regulate the amount of dry gas that passes through the humidifier (D-F) or bypasses to the adiabatic mixer (E-F). After entering the test section, the gas-mixture relative humidity is continuously measured with a hygrometer (HX92AV-RP1, Omega). The hygrometer output signal provides feedback to a PID control loop programmed in LabVIEW. All signals are acquired using a data acquisition system (PCI-6120, National Instruments). The control system is capable of maintaining a relative humidity in a range from 20% to 75% with a measurement uncertainty of ±2.5% relative humidity.

The condensation test section shown in Figure 3.1.2. maintains the test sample surface at a controlled subcooling temperature enclosed within the humidity-controlled chamber. Figure 3.1.2 (a) shows an exploded view of the test section. All components are mounted to the cold plate, which provides a constant base temperature for the attached thermoelectric cooler (ZT8, Laird Technologies). The thermoelectric cooler and temperature controller (MTTC-1410, Laird Technologies) are used for fine adjustment of the sample surface temperature. An aluminum block is attached to the top side of the thermoelectric cooler. Double-sided carbon conductive tape (PELCO Image Tabs) is used to affix the sample on top of the aluminum block. The thermoelectric cooler and the aluminum block assembly is pressed against the cold plate by a thermally insulating (polyether ether ketone, PEEK) shroud (k = 0.25 W/m K).

The test sample assembly is enclosed in a 10 cm × 10 cm × 7 cm acrylic chamber. The chamber is equipped with gas inlet/outlet ports, a condensate liquid drain, and two glass windows for viewing in directions normal (Figure 3.1.2 (b)) and parallel to the sample surface. A perforated gas diffuser plate is placed at the bottom of the chamber, in between the inlet and outlet ports, to evenly distribute the flow into the chamber. In order to assess the influence of species convection versus diffusion to the surface during the condensation experiments, an estimate of the air velocity inside the chamber is provided in Appendix E.

Four 0.5 mm-diameter T-type thermocouples (TMTSS-M050, Omega) are placed flush with the top surface of the aluminum block in notches. The surface temperature of the sample is assumed to be approximately equal to the average of these four temperature measurements. The temperature inside the chamber is monitored with a rake of three thermocouples evenly spaced 5 mm apart, with the closest thermocouple being 10 mm from the surface. The reading from the thermocouple furthest away from the surface is taken as the temperature of the ambient gas mixture. The reported surface subcooling temperature is the difference between the ambient gas mixture temperature and the surface temperature. All thermocouple measurements are referenced to a constant-temperature bath (TRCIII, Omega) maintained at 0 ± 0.1 °C and are calibrated before testing to achieve a measurement uncertainty of ± 0.3 °C.

3.1.3 Experimental Procedure and Visualization

Each condensation experiment is performed at a specified relative humidity and surface subcooling temperature. After attaching the sample to the aluminum block, the chamber is sealed and purged with a continuous stream of dry nitrogen gas for approximately 20 min until the relative humidity stabilizes at 10%. Simultaneously, the chiller circulates coolant to cool down the entire test section until the temperature of the surface and the gas mixture inside the chamber stabilize at ~20 °C.

After this initial conditioning, the gas mixture flow circuit controller is turned on with the desired set-point relative humidity. After ~10 min, the relative humidity measured inside the chamber reaches a steady value within ±5% error relative to the set-point value. Subsequently, the thermoelectric cooler controller is turned on; after 3 min, the temperature at the surface reaches a constant value within ±2% of the set-point temperature. By this procedure, condensation only begins when the surface temperature drops below the dew-point temperature as controlled by the fast-response thermoelectric stage, and after the chamber relative humidity and ambient temperature have already been stabilized.

A sequence of snapshot images normal to the surface are acquired every 30 s at 150× magnification using a long-focal-distance zoom lens (VH-Z50L, Keyence) with in-line illumination. The camera (FASTCAM 1024–PCI, Photron) and test section are mounted to micrometer stages to allow easier focusing on the surface of the sample. The spatial resolution was calibrated by measuring the grid pattern size of a calibration target (R1L3S3P Grid Distortion Target, ThorLabs). At 150× magnification, the spatial resolution is 3.99 ± 0.6 μm/pixel.

An automated image post-processing script was developed in MATLAB to recognize and characterize the size of droplets on the surface. The MATLAB script and a detailed description are provided in Appendix B. Figure 3.1.3 shows the processing steps for a representative image. The contrast-enhanced raw images (Figure 3.1.3 (a)) are segmented to a binary image (Figure 3.1.3 (b)). Unphysical internal boundaries caused by light reflection off the droplets are eliminated in a two-step process: the binary color scheme is first reversed and then each group of pixels that cannot be connected with the background (*i.e.*, a black dot inside a white spot) is filled. Each remaining circle that corresponds to a droplet is tagged based on the Hough transform technique [18] for edge recognition (Figure 3.1.3 (c)). The recognized circular boundaries are shown overlaid on the original image in Figure 3.1.3 (d). The radius and location of each droplet allows for identification of the total number of droplets present in each image. Also, by using the tagged identity of each droplet, the algorithm is capable of tracking single droplet growth in a set of sequential images.

3.2 Results and Discussions

3.2.1 Droplet Growth Regimes

A detailed description of the condensation dynamics for an illustrative experimental condition (RH = 70 % and ΔT_{sub} = 15 °C) provides a framework for comparison across different relative humidities. The condensation dynamics of the different droplet growth regimes are quantitatively assessed based on evolution of droplet size distribution, surface coverage, and average radius of condensate droplets.

Figure 3.2.1(a) shows histograms of the droplet size distribution on the surface with corresponding inset images of the droplets. Each selected image exhibits the unique characteristics within the different regimes. At the magnification and frame rate used for visualization in the experiments, we do not resolve a pure regime (*i*) where coalescence is absent. Droplet coalescence events are always present in the field of view between successive frames, and therefore the observed behavior is considered to begin within regime (*ii*). Regime (*ii*) is divided into sub-regimes (ii_{A}) and (ii_{B}) on account of contrasting growth dynamics.

During regime (ii_A) (t = 1.5 min) the surface is covered by a homogeneous pattern of small droplets with similar sizes in a narrow range of radii from 15 μm to 25 μm. As time proceeds, these droplets grow through two mechanisms: direct condensation on their liquid-gas interfaces, and coalescence. At some critical transition time, a significant change in the growth dynamics is realized. After this transition to regime (ii_B), at 12.5 min, the mean value of the distribution shifts to a larger radius (~50 μm) and coalescence effects significantly broaden the distribution by three times compared to the previous regime. Coalescence events in this second sub-regime contribute to the nucleation of new droplets in areas that were occupied by the original droplets prior to coalescence. Figure 3.2.1(b) shows a time series of images for an example coalescence of two droplets (dashed circles) that leads to the nucleation of a new smaller droplet. Since this new droplet grows in close proximity to the large, coalesced droplet, it soon thereafter merges into the large drop, as is shown in the last image in the time series.

In regime (*iii*) (t = 50 min), the average distance between the large coalesced droplets increases, leading to spontaneous nucleation of new droplets in the bare spaces between the larger droplets. These new droplets exist for a comparatively longer time before merging with neighboring droplets, and as a result, the size distribution splits into two characteristic groups of droplets: the first has a narrow distribution at a small radius (~25 µm) as characteristic of regime (ii_A), and the second has a larger mean droplet radius with a wider variation in radius size as characteristic of regime (ii_B). Such a bimodal distribution has been previously reported [19],[20], and the behavior seen in regime (*iii*) is generally consistent with observations in the literature.

Lastly, the larger droplets reach a critical size and slide off the surface by gravity. Small droplets nucleate in the freshly exposed area, initiating a new condensation cycle, and the peak in the bimodal distribution at small radii becomes more pronounced. Similar characteristics were observed during subsequent growth and sweeping cycles; however, time periodicity of the cycle cannot be assessed based on this global distribution pattern due to the coexistence of multiple generations of droplets within the same field of view.

3.2.2 Growth of Temporal-Average Radius

The droplet pattern characteristics within each regime can also be described in terms of the evolution of the average droplet radius ($<R>$) and the surface coverage (ε) with time, as shown in Figure 3.2.2 for a representative relative humidity. During regime (*ii*) ($t <$ 40 min) the average radius increases with time in accordance with a power law of the form $<R>\sim t^{\mu_{ii}}$. In regime (*iii*), (40 min $< t <$ 87.5 min) the average droplet radius and the surface coverage reach constant values at $<R>\approx$ 117 μm and ε ≈ 55%, respectively. At the end of regime (*iii*), the droplets slide off the surface, and a new generation of droplets begins to grow.

The transition between each regime is quantitatively defined based on a distinct change in the average-radius growth behavior. Figure 3.2.3 shows a logarithmic plot for the evolution of the droplet average radius. The dashed lines overlaid on the plot indicate fits to power laws of the form $<R>\sim t^{\mu_{ii}}$ over the durations of each regime. A distinct change in μ_{ii} determines the transitions.

A change in the power-law exponent within regime (*ii*) is clearly observed, and points to the need for subdivision of this regime. The transition occurs at t_1 = 2 min when the power-law exponent sharply changes from $\mu_{ii,A}$ = 0.27 in regime (ii_A) to $\mu_{ii,B}$ = 0.60 in regime (ii_B). While this distinction of growth behavior within regime (*ii*) has not been previously observed in the literature for experiments performed at high relative humidity, some quantitative comparisons against prior observations may be drawn. Since the size distribution of droplets present on the surface during regime (ii_A) is very narrow, the behavior of average radius growth in regime (ii_A) is found comparable to previously reported values for single droplet growth during regime (*ii*) in the literature (μ ≈ 1/3) [11,13,17]. The behavior of average radius growth for regime (ii_B) can be directly compared to previously reported values for average radius growth in regime (*ii*) in the literature ($\mu_{ii}\approx$ 0.75) [11-[13]. This observed drastic difference in the radius growth behavior between regime (ii_A) and (ii_B) may therefore be attributed to the respective dominance of growth by direct condensation versus coalescence of droplets, as is investigated further in subsequent sections.

The transition into regime (*iii*) in Figure 3.2.3 occurs at t_2 = 40 min; as the droplets become dispersed and the frequency of coalescence events is reduced, the rate of radius growth by direct condensation on large droplets is comparatively small (μ_{iii} = 0.11). Finally, droplets sliding off the surfaces marks the end of regime (*iii*) at t_3 = 87.5 min.

3.2.3 Effect of Relative Humidity on Temporal-Average Radius

These unique average-radius growth dynamics in regime (*ii*) are further assessed as a function of relative humidity (RH = 45%, 50%, 55%, and 70%) for a constant surface subcooling temperature (ΔT_{sub} = 15 °C). Figure 3.2.4 shows a logarithmic plot of the average radius versus time for the four different relative humidity cases. Power-law fits to the data were used to assess the growth behavior, and to quantitatively determine the regime transition points t_1 and t_2. Figure 3.2.5 shows the dependence of the power-law exponents with relative humidity during regimes (ii_A) and (ii_B).

During regime (ii_A), the power-law rate of growth exponent increases with relative humidity from $\mu_{ii,A}$ = 0.12 at RH = 45% to $\mu_{ii,A}$ = 0.27 at RH = 70%. This is indicated by the increased slope at higher relative humidity in Figure 3.2.4. As a result, the time of the transition to regime (ii_B), which occurs at a consistent average radius size, is delayed for lower relative humidity (*e.g.,* from t_1 = 2.0 min at RH = 70% to t_1 = 6.5 min at RH = 45%). Conversely, relative humidity has little influence on the condensation dynamics when coalescence appears to be the dominant mechanism in regime (ii_B); variation in

$\mu_{ii,B}$ is negligible for relative humidity ranging from 45% to 70%. The following section analyzes single-droplet growth mechanisms to explain these trends observed with relative humidity, which indicate that the appearance and persistence of regime (ii_A) is amplified at lower relative humidity.

3.2.4 Single Droplet Growth

Tracking the evolution of single condensate droplets on the surface confirms the predominant mechanisms leading to the contrasting trends in average radius growth within regime (*ii*). Figure 3.2.6 shows the radius of one representative droplet over time at a relative humidity of 50%. Growth is characterized by periods of direct condensation on the droplet surface and intermittent coalescence events. Four coalescence events occur in the lifetime of the droplet shown in Figure 3.2.6, and are characterized by a sudden increase in the radius of the droplet. The periods of direct condensation are characterized by power-law growth with slower absolute rates of growth as the droplet radius increases. At early stages of growth, the step changes upon coalescence are a comparatively smaller percentage of the radius growth rate by direct condensation, and therefore direct condensation governs the average-radius growth dynamics. At later stages within regime (*ii*), these increments are comparatively larger and the growth by direct condensation is also slower at larger droplet radii. Droplet coalescence dominates the average radius growth dynamics at these later times within regime (*ii*).

The power-law exponent describing average radius growth was only observed to be dependent on relative humidity in regime (ii_A), where single droplet growth by direct condensation is predominant. This suggests that the relative humidity influences the behavior of single-droplet growth within an array of densely packed droplets at the early stages of growth. Other studies have previously indicated that single droplet growth-law exponents are sensitive to boundary conditions that influence the pattern of vapor mass flow to the surface from the surroundings [14]. To assess the influence of relative humidity on the growth only by direct condensation on the droplet interfaces (excluding growth by coalescence), the condensation mass flux on the interfaces of the individual droplets is calculated based on the instantaneous rate of change of droplet radius (omitting step changes due to coalescence). Figure 3.2.7 shows a plot of the condensation mass flux on the interfaces of single droplets as a function of the droplet size for each relative humidity tested (averaged across all droplets present on the surface). In all of the cases, the mass flux decreases as the droplet size increases. This indicates the importance of the thermal resistance of the droplet at all relative humidities tested; larger droplets impose a larger thermal resistance between the solid substrate and liquid-vapor interface of the droplet, thereby effectively reducing the subcooling below ambient at the interface. However, a significant change in the behavior is noted for the lower values of relative humidity tested (45% and 50%). The mass flux dependence on radius is weaker, suggesting that vapor species diffusion becomes an important rate-limiting transport mechanism at low relative humidity that could alter the vapor species concentration profile in the ambient, and accordingly the growth-law exponent. Figure 3.2.7 also clearly indicates the strong dependence of the absolute magnitude of the single droplet condensation mass flux on the relative humidity.

3.2.5 Condensation Behavior with Time

A primary concern of applications relying on dropwise condensation of water vapor may often be the volumetric rate of condensation on the surface. Figure 3.2.8 (a) describes the characteristic evolution of the volumetric condensation rate on the surface based on a selected case, with the droplet growth regimes overlaid. The data presented have been smoothed using a moving-average filter to reduce the noise associated with calculating a time rate of change from discrete data points. In general, the condensation rate first decreases and then increases in time. The trends in overall rate of condensation on the surface can be explained by the size effects in single droplet growth (Figure 3.2.7) and the droplet size distribution on the surface (Figure 3.2.8 (b)).

At early times in regime (ii_A) (t = 3 min), a uniform population of small droplets primarily contribute to the overall condensation rate. The condensation rate decreases sharply as the average size of the droplets present on the surface increases (t = 6 min), and is consistent with the single droplet size effect shown previously in Figure 3.2.7.

As time proceeds into growth regime (ii_B) (t = 10 min), the average distance between the larger droplets increases, and coalescence events spawn new droplets with small radii, as was described above with reference to Figure 3.2.1 (b). While coalescence events that create larger droplets would otherwise be expected to reduce the condensation rate, this population of new droplets with $R \lesssim 50$ μm yield a net increase in the rate of condensation on the surface. As time proceeds, the size difference between small and the large droplets widens and the average condensation rate stabilizes. At this stage, small droplets that nucleate have an even greater influence on the overall rate. Each coalescence event between large droplets spurs the nucleation of many small droplets that then causes large fluctuations in the condensation rate on the surface (*e.g.*, t = 40 min).

The evolution of the volumetric condensation rate is shown for all the relative humidities tested in Figure 3.2.9. In general, the condensation rate is faster for higher relative humidity. At higher relative humidity, the initial reduction in the condensation rate with time is less pronounced and exists for a shorter period (or is suppressed entirely in the case of 70% relative humidity). Also, as described above, a transition from the initially decreasing to an increasing condensation rate is determined by the nucleation and growth of small interstitial droplets after coalescence events. Higher relative humidities are able to support nucleation at lower interstitial spacing upon coalescence of smaller droplet radii [19], whereas nucleation of interstitial droplets is suppressed for longer periods at low relative humidity. Low relative humidities thereby prolong the period of single droplet-like growth behavior that has a reducing condensation rate with time. Understanding these interdependent transport mechanisms during condensation, and engineering surfaces/systems that eliminate such low-performance transients, is key to the deployment of systems that condense vapor at low relative humidity.

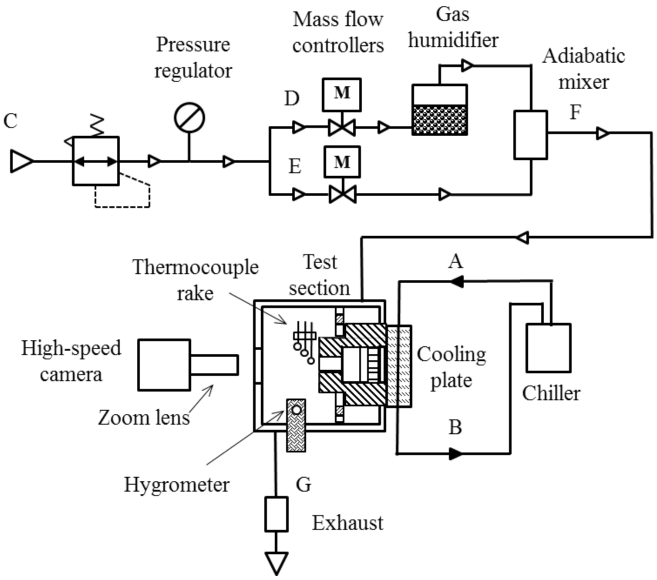

Figure 3.1.1 Schematic diagram of nitrogen-water gas mixture and chilled water flow circuits.

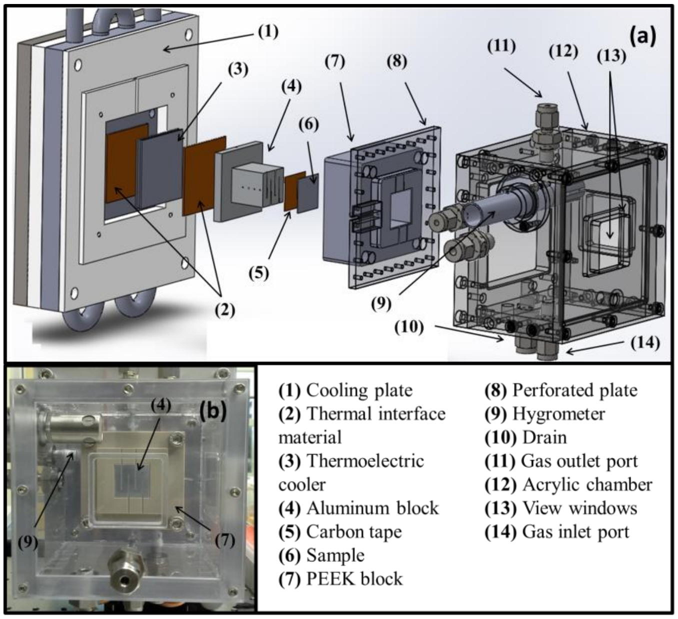

Figure 3.1.2 (a) 3D CAD model of the test section exploded assembly, and (b) front view photograph of the chamber.

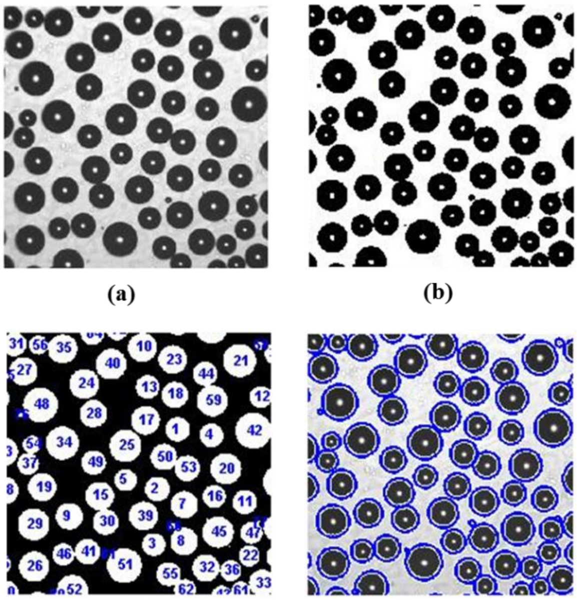

(a) (b)

(c) (d)

Figure 3.1.3 Example image subject to post-processing by (a) contrast enhancement, (b) binary segmentation, (c) color scheme reversal, elimination of unphysical reflections, and droplet tagging, and (d) circular droplet boundary detection (RH = 70%; ΔT_{sub} = 15 °C, t = 15.5 min).

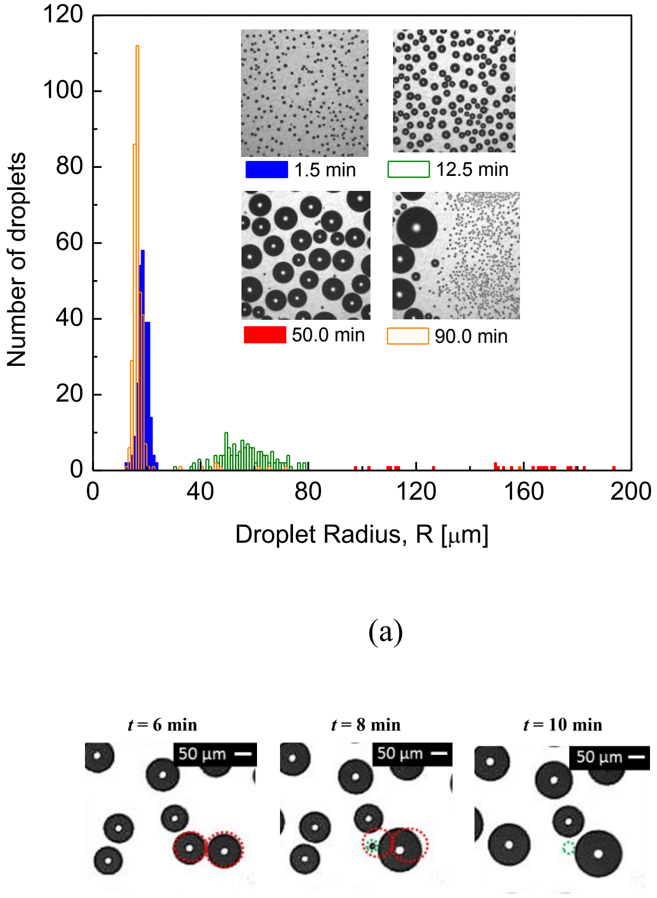

(a)

(b)

Figure 3.2.1 (a) Histogram of number of droplets at a given size at $t = 1.5$, 12.5, 50, and 90 min. Inset images show condensed droplets on the substrate. (b) The set of bottom images depicts a coalescence event in regime (ii_B). ($RH = 70\%$; $\Delta T_{sub} = 15$ °C.)

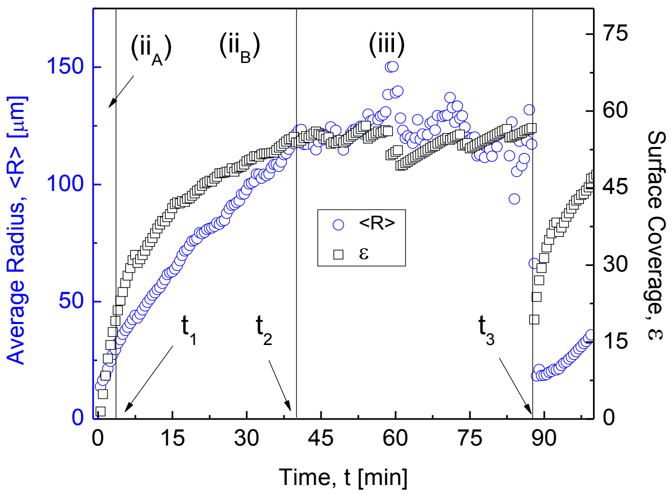

Figure 3.2.2 Average radius (left axis) and surface coverage (right axis) versus time for RH = 70% and ΔT_{sub} = 15 °C.

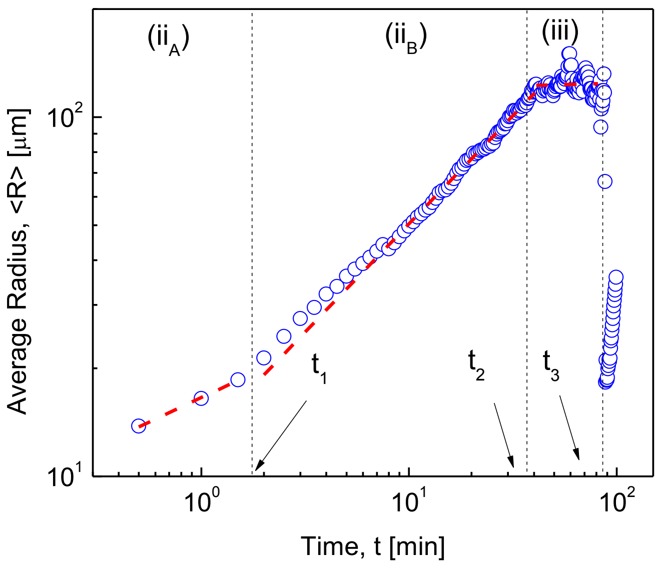

Figure 3.2.3 Average radius versus time for RH = 70% and ΔT_{sub} = 15 °C. Dashed lines indicate power-law fits within each regime.

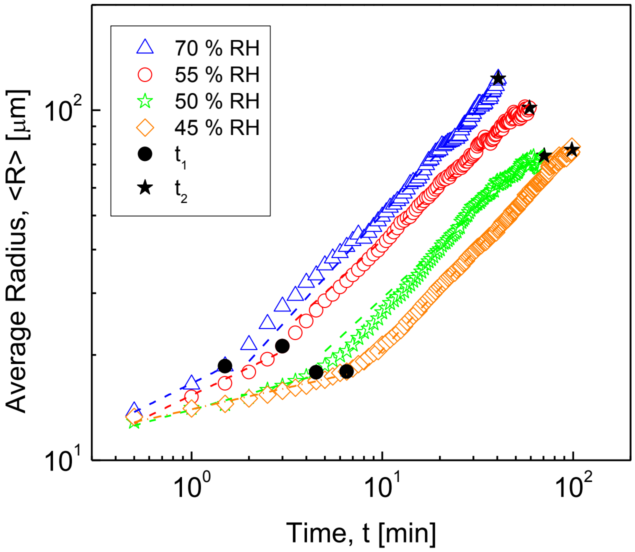

Figure 3.2.4 Average radius versus time at ΔT_{sub} = 15 °C and 70%, 55%, 50%, and 45% relative humidity.

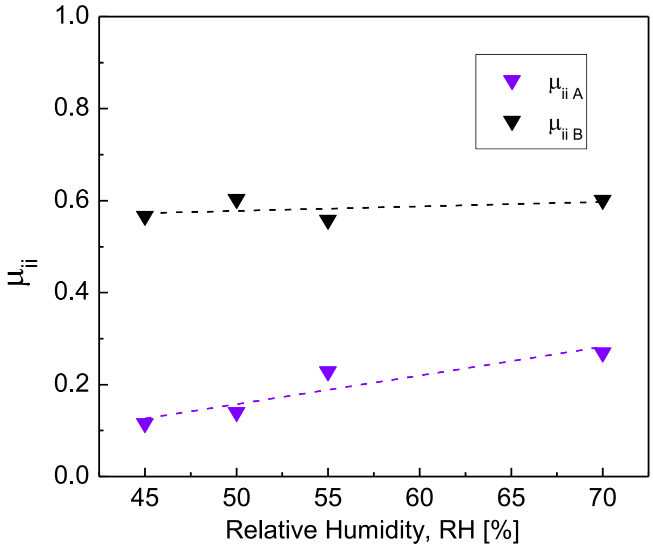

Figure 3.2.5 Exponent of the power-law fit to the temporal average radius data of the form $<R>\sim t^{\mu}$ for regime (ii_A) ($\mu_{ii,A}$) and regime (ii_B) ($\mu_{ii,B}$) as a function of relative humidity.

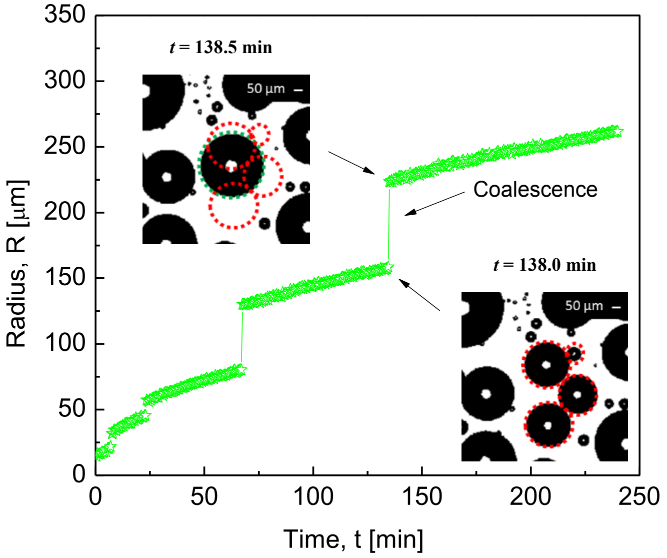

Figure 3.2.6 Radius versus time for a single droplet at ΔT_{sub} = 15 °C and 50% relative humidity. Inset images show a set of droplets before and after the last coalescence event.

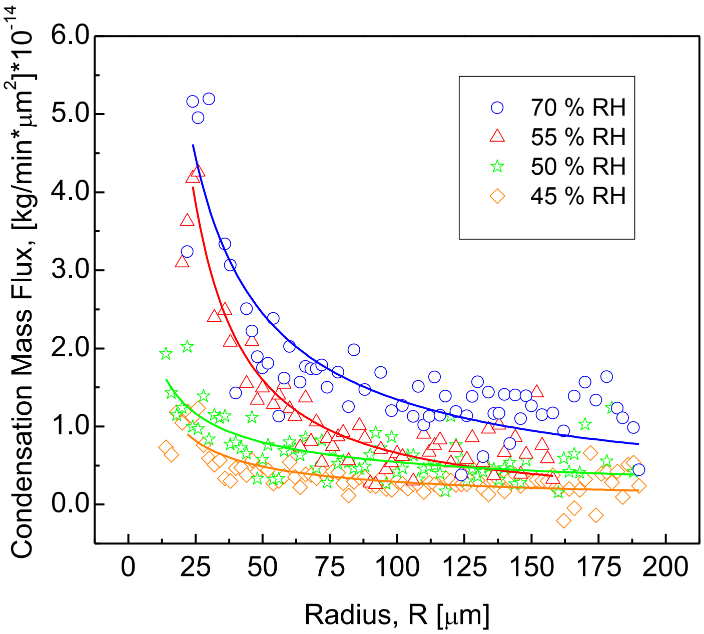

Figure 3.2.7 Rate of condensation per unit surface area of a single droplet as a function of droplet radius at ΔT_{sub} = 15 °C and 70%, 55%, 50%, and 45% relative humidity.

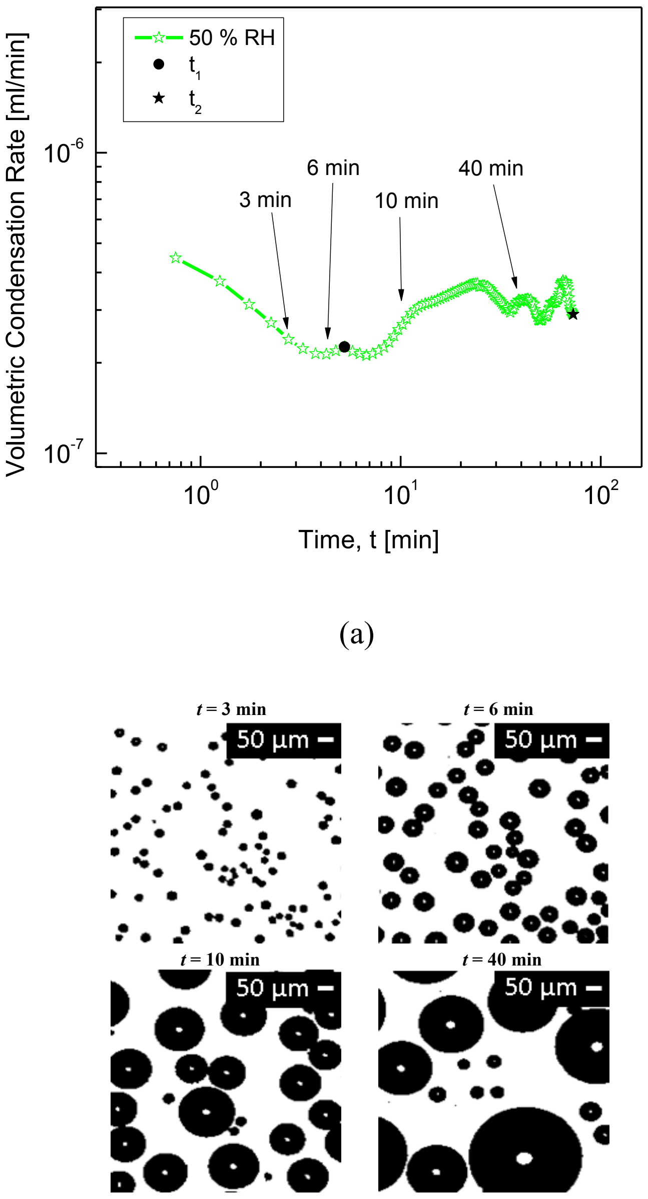

(a)

(b)

Figure 3.2.8 (a) Volumetric rate of condensation on the surface as function of time, and (b) time series of images of the droplets on the surface for ΔT_{sub} = 15 °C and 50% relative humidity.

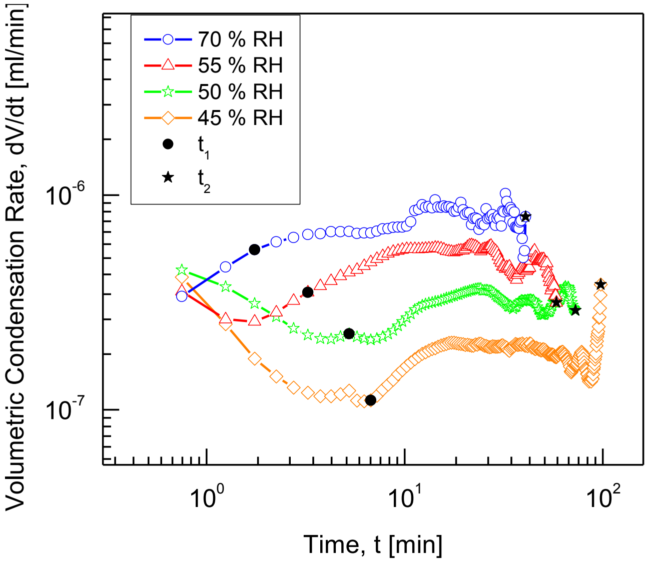

Figure 3.2.9 Volumetric rate of condensation on the surface as a function of time at ΔT_{sub} = 15 °C and 70%, 55%, 50%, and 45% relative humidity.

CHAPTER 4. CONCLUSIONS AND FUTURE WORK

This chapter summarizes the key findings of the effects of relative humidity on dropwise condensation dynamics. Several potential future research directions have emerged from this work and are proposed.

4.1 Conclusions

In this thesis, the growth of water droplets on a smooth hydrophobic surface was investigated at different ambient relative humidities. A detailed experimental investigation was carried out using a test facility that controls relative humidity in a condensation test section by automatically metering the influx of dry and moist air. The characteristic behavior of the early stages of droplet growth, before surface coverage parameters reached constant values, were analyzed as a function of the relative humidity. The growth of the average droplet radius versus time was suitably described by a power law in an initial regime that was characterized by a narrow distribution of small droplets; average growth behaved similarly to single-droplet growth and the exponent of the power law was sensitive to relative humidity in this regime. In the subsequent regime, coalescence dominated the average-radius growth dynamics, which were insensitive to relative humidity. Further interrogation of single-droplet radius growth, after filtering out the contribution of coalescence effects, confirmed these dependencies on relative humidity.

A strong dependence of the droplet size on the condensation mass flux on the interfaces of single droplets was observed (higher rates at smaller droplet sizes). This size dependence of the condensation rate was used to explain the temporal evolution of the overall volumetric condensation rate on the surface. As a generation of droplets grows on the surface, the condensation rate decreases as the droplets grow and coalesce. This trend does not reverse until the distribution of droplets becomes sparse enough that coalescence events induce nucleation of new small droplets on the surface, which increase the net condensation rate. This behavior is shown to be highly sensitive to the relative humidity. The surface is more easily starved of water vapor in the droplet interstices at lower ambient relative humidity. This prolongs and amplifies the period of reduced condensation rates on the surface. In light of the experimental evidence presented in this document, the growth of droplets during dropwise condensation process is revealed to be highly sensitive to change in relative humidity, which must be considered in the practical design of condenser surfaces and systems.

4.2 Suggestions for Future Work

4.2.1 Growth of Micro-Drops on Structured Superhydrophobic Surfaces

There is an increasing interest in dropwise condensation on structured superhydrophobic surfaces due to the potential for greatly enhanced heat and mass transfer rates compared to flat hydrophobic surfaces. Investigation of the droplet size distribution, performed by Dietz *et al.* [34] using an environmental scanning electron microscopy (ESEM), revealed superhydrophobic surfaces generated departure of droplets at smaller sizes compared with hydrophobic surfaces. As a result, the droplet size distribution shifted to smaller sizes, indicative of potentially greater heat transfer coefficients.

Experimental and modeling work investigating the mechanisms that govern the dynamics of growth at the microscale (~10 μm) suggest that droplets growing in limited contact with the surface (Cassie state) [41] exhibited a high thermal resistance detrimental to heat transfer [58]. Recent experiments with enhanced spatial and temporal resolution performed by Rykaczewski *et al.* [35,57] showed microscale droplets would initially grow in a constant base mode, contrary to previous reports by Kim and Kim [10] and Miljkovic *et al.* [58], in which the initial growth mechanism was in the constant contact angle mode.

Additional experimental work is needed to understand the influence of surface morphologies on the growth mechanism realized. High spatial resolution ESEM visualization at controlled vapor pressure and surface temperature could help to further elucidate the dynamics of microscale droplet growth.

4.2.2 Effects of Droplet Spacing and the Surrounding Vapor Distribution on Single-Droplet Growth Dynamics

Previous reports have demonstrated that single-droplet condensation/evaporation is affected by any boundary conditions that affect the local surrounding species concentration of vapor. For a densely packed array of drops, the volume of each individual drop will shrink or grow proportionally with time as $R \sim t^{1/3}$. In the case of an isolated drop, however, the volume growth will change accordingly to $R \sim t^{1/2}$. As the distance between the drops within an array increases, the exponent of the power law varies from 0.3 to 0.5. Sokuler *et al.* [31] simulated single-droplet growth by solving the diffusion equation with symmetric boundary conditions that emulated a periodic array of droplets. Their results indicated the transition in the power-law exponent would occur when inter-drop spacing is of the same order as the distance above the surface at which the vapor pressure reaches the ambient value. Thus, the vapor distribution of the droplet's surrounding dominates the rate of growth when the spacing is less than this distance.

The influence of spacing on droplet growth is further complicated when the population of drops has a non-uniform size or irregular distribution. Schäfle *et al.* [59] reported evaporation dynamics of volatile liquid drops organized in a hexagonally shaped array; large droplets in the vicinity of smaller ones grow by engulfing smaller droplets. Leach *et al.* [19], observed that small drops located in close proximity (~13 µm) to large drops grew at growth rates 20% slower than droplets of similar size located at further distances (~50 µm). Ucar and Erbil [60] used the diffusion equation to compare single droplet rates of growth on surfaces with different roughness. They found that single droplet rates of growth decreased between 14-40% when the drop density on the surface was increased (as a result of greater surface roughness). They attribute these discrepancies to lateral blocking of vapor diffusion caused by neighboring droplets.

Further investigations on the condensation/evaporation of drops is necessary to study the effect of inter-drop spacing and droplet size on the growth dynamics as function of ambient vapor partial pressure.

4.2.3 Surface Design for Enhanced Heat and Mass Transfer During Condensation of Humid Air

When condensation occurs in presence of air, dropwise condensation may only offer similar rates of heat transfer as compared to film-wise condensation [61] (contrary to the behavior in pure vapor where dropwise condensation yields drastically improved rates of heat transfer). Even small concentrations of non-condensable gases in water vapor can be severely detrimental to mass transfer rates (compared to pure vapor), due to the high thermal resistance of the air-rich layer that forms near the condensing surface [62].

To investigate the effect of surface wettability on mass transfer during condensation of humid air, Lee *et al.*[64] compared the amount of water collected for a wide range of surface wettabilities under similar conditions. Their results showed uniformly hydrophilic surfaces exhibited higher rates of water condensation and collection than surfaces with lower wettability. In comparison, fog basking applications were the most efficient when the surface consisted of hydrophilic islands surrounded by a hydrophobic background [65]. Surface engineering for water harvesting applications from humid air requires extensive investigation of the proper surface wettability design that can enhance water yield in harvesting systems.

An experimental investigation that evaluates the water collection efficiency using enhancement features can be performed under different environment conditions with the aim of revealing which features are most appropriated under different conditions.

LIST OF REFERENCES

LIST OF REFERENCES

[1] R. V. Wahlgren, “Atmospheric water vapour processor designs for potable water production: A review,” *Water Research*, vol. 35, no. 1, pp. 1–22, 2001.

[2] D. Milani, A. Abbas, A. Vassallo, M. Chiesa, and D. A. Bakri, “Evaluation of using thermoelectric coolers in a dehumidification system to generate freshwater from ambient air,” *Chemical Engineering Science*, vol. 66, no. 12, pp. 2491–2501, 2011.

[3] K. Hong and R. L. Webb, “Performance of dehumidifying heat exchangers with and without wetting coatings,” *Journal of Heat Transfer*, vol. 121, no. 4, pp. 1018−1026, 1999.

[4] S. Parekh, M. M. Farid, J. R. Selman, and Said Al-hallaj, “Solar desalination with a humidification-dehumidification technique: A comprehensive technical review,” *Desalination*. vol. 160, pp. 167–186, 2004.

[5] L. Pérez-Lombard, J. Ortiz, and C. Pout, “A review on buildings energy consumption information,” *Energy and Buildings*, vol. 40, no. 3, pp. 394–398, 2008.

[6] J.W. Rose, “Dropwise condensation theory and experiment: A review,” *Proceedings of the Institution of Mechanical Engineers, Part A: Journal of Power and Energy*, vol. 216, no. 2, pp.115–128, 2002.

[7] J. B. Boreyko and C.-H. Chen, “Self-propelled dropwise condensate on superhydrophobic surfaces,” *Physical Review Letters*, vol. 103, no. 18, 184501, 2009.

[8] R. Enright, N. Miljkovic, J. L. Alvarado, K. Kim, and J. W. Rose, “Dropwise Condensation on Micro- and Nanostructured Surfaces,” *Nanoscale and Microscale Thermophysical Engineering*, vol. 18, no. 3, pp. 223–250, 2014.

[9] P. Dimitrakopoulos and J. J. L. Higdon, “On the gravitational displacement of three-dimensional fluid droplets from inclined solid surfaces,” *Journal of Fluid Mechanics*, vol. 395, pp. 181–209, 1999.

[10] H. Y. Kim, H. J. Lee, and B. H. Kang, “Sliding of liquid drops down an inclined solid surface,” *Journal of Colloid and Interface Science*, vol. 247, no. 2, pp. 372–380, 2002.

[11] D. Beysens and C. M. Knobler, “Growth of breath figures,” *Physical Review Lett*ers, vol. 57, no. 12, pp. 1433–1436, 1986.

[12] J. L. Viovy, D. Beysens, and C. M. Knobler, “Scaling description for the growth of condensation patterns on surfaces,” *Physical Review A*, vol. 37, no. 12, pp. 4965–4970, 1988.

[13] D. Fritter, C. M. Knobler, and D. A. Beysens, “Experiments and simulation of the growth of droplets on a surface (breath figures),” *Physical Review A*, vol. 43, no. 6, pp. 2858–2869, 1991.

[14] A. Steyer, P. Guenoun, D. Beysens, and C. M. Knobler, “Growth of droplets on a substrate by diffusion and coalescence,” *Physical Review A*, vol. 44, no. 12, pp. 8271–8277, 1991.

[15] D. Beysens, “The formation of dew,” *Atmospheric Research*, vol. 39, no. 1–3, pp. 215–237, 1995.

[16] J. Blaschke, T. Lapp, B. Hof, and J. Vollmer, “Breath figures: nucleation, growth, coalescence, and the size distribution of droplets,” *Physical Review Letters*, vol. 109, no. 6, 068701, 2012.

[17] M. Mei, B. Yu, M. Zou, and L. Luo, “A numerical study on growth mechanism of dropwise condensation,” *International Journal of Heat and Mass Transfer*, vol. 54, no. 9–10, pp. 2004–2013, 2011.

[18] T. J. Atherton and D. J. Kerbyson, “Size invariant circle detection,” *Image and Vision Computing*, vol. 17, no. 11, pp. 795–803, 1999.

[19] R. N. Leach, F. Stevens, S. C. Langford, and J. T. Dickinson, “Dropwise condensation: experiments and simulations of nucleation and growth of water drops in a cooling system,” *Langmuir*, vol. 22, no. 21, pp. 8864–8872, 2006.

[20] A. M. Macner, S. Daniel, and P. H. Steen, “Condensation on surface energy gradient shifts drop size distribution toward small drops,” *Langmuir,* vol. 30, no. 7, pp. 1788–1798, 2014.

[21] E. Schmidt, W. Schurig and W. Sellschopp, “Versuche über die condensation von wasserdampf in film – and tropfenform,” *Technische Mechanik und Thermodynamik*, 1, pp. 53-63, 1930.

[22] C. Graham, and P. Griffith, “Drop size distributions and heat transfer in dropwise condensation,” *International Journal of Heat and Mass Transfer*, vol. 16, no 2, pp. 337-346, 1973.

[23] L.C.F. Blackman, and M.J.S. Dewar, “Promoters for the dropwise condensation of steam,” Journal of Applied Chemistry, vol. 7, no. 4, pp. 160-171, 1957.

[24] R. Wilmshurst, and J.W. Rose, “Dropwise and filmwise condensation of aniline, ethanediol and nitrobenzene,” *Proceedings of the 5th International Heat Transfer Conference,* Tokyo, Japan, pp. 269-273, 1974.

[25] R. A. Sigsbee, “Nucleation” (A. C. Zettlemoyer ed, Marcel Dekker, New York, 1969).

[26] J. L. McCormick and J. W. Westwater, “Nucleation sites for dropwise condensation”. *Chemical Engineering Science*, vol. 20, no. 12, pp. 1021–1031, 1965.

[27] M. Ichikawa, N. Magome, and K. Yoshikawa, “Rhythmic growth and collapse of a micro water droplet,” *Europhysics Letters* , vol. 66, no. 4, p. 545, May 2004.

[28] H. Zhao and D. Beysens, “From droplet growth to film growth on a heterogeneous surface: condensation associated with a wettability gradient,” *Langmuir*, vol. 11, no. 2, pp. 627–634, 1995.

[29] I. O. Fritter and H. Y. Erbil, “Use of diffusion controlled drop evaporation equations for dropwise condensation during dew formation and effect of neighboring droplets,” *Colloids and Surfaces A: Physicochemical and Engineering Aspects*, vol. 411, pp. 60–68, 2012.

[30] B. J. Briscoe and K. P. Galvin, “An experimental study of the growth of breath figures,” *Colloids and Surfaces*, vol. 56, pp. 263–278, 1991.

[31] M. Sokuler, G. K. Auernhammer, C. J. Liu, E. Bonaccurso, and H.-J. Butt, “Dynamics of condensation and evaporation: Effect of inter-drop spacing,” *Europhysics Letters*, vol. 89, no. 3, p. 36004, 2010.

[32] E.J. Le Fevre, J.W. Rose, “A theory of heat transfer by dropwise condensation”, *Proceedings of 3rd International Heat Transfer*, vol. 2, pp. 362–375. 1966.

[33] N. Watanabe, M. Aritomi, and A. Machida, “Time-series characteristics and geometric structures of drop-size distribution density in dropwise condensation,” *International Journal of Heat and Mass Transfer*, vol. 76, pp. 467–483, 2014.

[34] C. Dietz, K. Rykaczewski, A. G. Fedorov, and Y. Joshi, “Visualization of droplet departure on a superhydrophobic surface and implications to heat transfer enhancement during dropwise condensation,” *Applied Physics Letters*, vol. 97, no. 3, pp, 2010.

[35] K. Rykaczewski, “Microdroplet Growth mechanism during water condensation on superhydrophobic surfaces,” *Langmuir*, vol. 28, no. 20, pp. 7720–7729, 2012.

[36] S. Khandekar, K. Muralidhar. “Dropwise condensation on inclined textured surfaces”. *Springer Briefs in Applied Sciences and Technology*; Springer: New York, 2014.

[37] B. S. Sikarwar; N. K. Battoo, S. Khandekar, “Dropwise condensation underneath chemically textured surfaces: simulation and experiments”. *Journal of Heat Transfer*, vol.133, pp. 021501 (15), 2011.

[38] H. Tanaka, “Measurements of drop-size distributions during transient dropwise condensation”. *Journal of Heat Transfer*, vol. 97, no. 3, pp. 341−346, 1975.

[39] S. Daniel, M. K. Chaudhury, J. C Chen, “Fast drop movements resulting from the phase change on a gradient surface.” *Science*, vol. 291, pp. 633−636, 2001

[40] C. Lv and P. Hao, “driving droplet by scale effect on microstructured hydrophobic surfaces,” *Langmuir*, vol. 28, no. 49, pp. 16958–16965, 2012.

[41] C. Dorrer and J. Rühe, “Condensation and wetting transitions on microstructured ultrahydrophobic surfaces”, *Langmuir,* vol. 23, no. 7, p. 3820–3824, 2007.

[42] Y.-T. Cheng and D. E. Rodak, “Is the lotus leaf superhydrophobic?,” *Applied Physics Letters*, vol. 86, no. 14, p. 144101, 2005.

[43] S. C. Thickett, C. Neto, and A. T. Harris, “Biomimetic surface coatings for atmospheric water capture prepared by dewetting of polymer films,” *Advanced Materials*., vol. 23, no. 32, pp. 3718–3722, 2011.

[44] J. Cheng, A. Vandadi, and C.-L. Chen, “Condensation heat transfer on two-tier superhydrophobic surfaces,” *Applied Physics Letters*, vol. 101, no. 13, p. 131909, Sep. 2012.

[45] C.-H. Chen, Q. Cai, C. Tsai, C.-L. Chen, G. Xiong, Y. Yu, and Z. Ren, “Dropwise condensation on superhydrophobic surfaces with two-tier roughness,” *Applied Physics Letters*, vol. 90, no. 17, p. 173108, Apr. 2007.

[46] Y. C. Jung and B. Bhushan, “Wetting behaviour during evaporation and condensation of water microdroplets on superhydrophobic patterned surfaces,” *Journal of Microscopy*, vol. 229, no. Pt 1, pp. 127–140, 2008.

[47] J. Feng, Y. Pang, Z. Qin, R. Ma, and S. Yao, “Why condensate drops can spontaneously move away on some superhydrophobic surfaces but not on others,” *ACS Applied Materials and Interfaces*, vol. 4, no. 12, pp. 6618–6625, 2012.

[48] R. D. Narhe, M. D. Khandkar, P. B. Shelke, A. V. Limaye, and D. A. Beysens, “Condensation-induced jumping water drops,” *Physical Review E*, vol. 80, no. 3, p. 031604, 2009.

[49] T. Q. Liu, W. Sun, X. Y. Sun, and H. R. Ai, “Mechanism study of condensed drops jumping on super-hydrophobic surfaces*,” Colloids and Surfaces A: Physicochemical and Engineering Aspects*, vol. 414, pp. 366–374, 2012.

[50] Y. Nam, H. Kim, and S. Shin, “Energy and hydrodynamic analyses of coalescence-induced jumping droplets,” *Applied Physics Letters*, vol. 103, no. 16, p. 161601, 2013.

[51] . B. Peng, S. Wang, Z. Lan, W. Xu, R. Wen, and X. Ma, “Analysis of droplet jumping phenomenon with lattice Boltzmann simulation of droplet coalescence,” *Applied Physics Letters*, vol. 102, no. 15, p. 151601, 2013.

[52] M. He, Q. Zhang, X. Zeng, D. Cui, J. Chen, H. Li, J. Wang, and Y. Song, “Hierarchical porous surface for efficiently controlling microdroplets’ self-removal,” Advanced Materials, vol. 25, no. 16, pp. 2291–2295, Apr. 2013.

[53] N. Miljkovic, R. Enright, Y. Nam, K. Lopez, N. Dou, J. Sack, and E. N. Wang, "Jumping-Droplet-Enhanced Condensation on Scalable Superhydrophobic Nanostructured Surfaces," *Nano Letters*, vol. 13, no. 1, pp. 179–187, 2013.

[54] X. Chen, J. Wu, R. Ma, M. Hua, N. Koratkar, S. Yao, and Z. Wang, "Nanograssed micropyramidal architectures for continuous dropwise condensation," *Advanced Functional Materials*, vol. 21, no. 24, pp. 4617–4623, 2011.

[55] D. Quéré, "Non-sticking drops," *Reports on Progress in Physics*., vol. 68, no. 11, pp. 2495, 2005.

[56] S. Anand, A. T. Paxson, R. Dhiman, J. D. Smith, and K. K. Varanasi, "Enhanced condensation on lubricant-impregnated nanotextured surfaces," *ACS Nano*, vol. 6, no. 11, pp. 10122–10129, 2012.

[57] K. Rykaczewski, A. T. Paxson, S. Anand, X. Chen, Z. Wang, and K. K. Varanasi, "Multimode multidrop serial coalescence effects during condensation on hierarchical superhydrophobic surfaces," *Langmuir*, vol. 29, no. 3. pp. 881-891, 2012.

[58] N. Miljkovic, R. Enright, and E. N. Wang, "Effect of droplet morphology on growth dynamics and heat transfer during condensation on superhydrophobic nanostructured surfaces," *ACS Nano*, vol. 6, no. 2, pp. 1776–1785, 2012.

[59] C. Schäfle, C. Bechinger, B. Rinn, C. David, and P. Leiderer, "Cooperative evaporation in ordered arrays of volatile droplets," *Physical Review Letters*, vol. 83, no. 25, pp. 5302–5305, 1999.

[60] I. O. Ucar and H. Y. Erbil, "Use of diffusion controlled drop evaporation equations for dropwise condensation during dew formation and effect of neighboring droplets," *Colloids and Surfaces A: Physicochemical and Engineering Aspects*, vol. 411, pp. 60–68, 2012.

[61] B. J. Chung, M. C. Kim, and M. Ahmadinejad, "Film-wise and drop-wise condensation of steam on short inclined plates*," Journal of Mechanical Science and Technology*, vol. 22, no. 1, pp. 127–133, 2008.

[62] D. W. Tanner, C. J. Potter, D. Pope, and D. West, "Heat transfer in dropwise condensation—Part I The effects of heat flux, steam velocity and non-condensable gas concentration," *International Journal of Heat and Mass Transfer, vol*. 8, no. 3, pp. 419–426, 1965

[63] D.W. Tanner, D. Pope, C.J. Potter and D. West, "Heat transfer in DWC at low steam pressure in the absence and presence of non-condensable gas", *International Journal of Heat and Mass Transfer*, vol. 11 no. 2, pp. 181–190, 1968.

[64] A. Lee, M.-W. Moon, H. Lim, W.-D. Kim, and H.-Y. Kim, "Water harvest via dewing," *Langmuir*, vol. 28, no. 27, pp. 10183–10191, 2012.

[65] R. P. Garrod, L. G. Harris, W. C. E. Schofield, J. McGettrick, L. J. Ward, D. O. H. Teare, and J. P. S. Badyal, "Mimicking a stenocara beetle's back for microcondensation using plasmachemical patterned superhydrophobic-superhydrophilic surfaces," *Langmuir*, vol. 23, no. 2, pp. 689–693, 2007.

[66] J. R. Taylor, "An Introduction to Error Analysis", 2nd Ed., University Science Books, 1997.

APPENDICES

Appendix A Condensation Experimental Facility

This appendix lists all of the experimental equipment used and the fabricated components of the condensation test facility, and CAD drawings for custom-made parts.

Table A-1 Equipment and Part List of the Condensation Test Facility

Item	Manufacturer/Supplier	Model
Optical Measurements		
High-speed camera	Photron USA, Inc.	FASTCAM 1024–PCI
Long-focal-distance zoom lens	Keyence	VH-Z50L
Temperature Measurement		
Thermocouples	Omega	TMTSS-M050
RTD sensor	Omega	PR-11-1-M15-(150)
High-stability ice point cell	Omega	TRCIII
Thermal Control Systems		
Water chiller	Thermo Scientific	ThermoFlex 900
Cold plate	Lytron	CP12
Thermoelectric cooler	Laird Technologies	ZT8
Thermoelectric cooler controller	Laird Technologies	MTTC-1410
Sample Fabrication		
Silicon wafer	University Wafer	UW447
Fluorinert liquid	3M	FC-77
Teflon solution	Dupont	AF 1600
Humidity Control System		
Mass flow controllers	Omega	FMQ 5400, 0-2 SLM
Hygrometer	Omega	HX92AV-RP1
Data acquisition system	National Instruments	PCI-6120

Table A-1 Continued.

Miscellaneous		
Conductive Carbon Tape	PELCO, Image Tabs	n/a
Data acquisition system	Agilent Technologies, Inc.	34970A
Linear stage	Parker-Hannifin Corp.	4414 ST B/S C MIC 5.0 SQ
Fabricated Facility Components		
Aluminum block	Thermophysical Research Laboratories, Inc.	Custom
Insulation block	Thermophysical Research Laboratories, Inc.	Custom
Perforated gas diffuser plate	Thermophysical Research Laboratories, Inc.	Custom
Acrylic chamber	Thermophysical Research Laboratories, Inc.	Custom

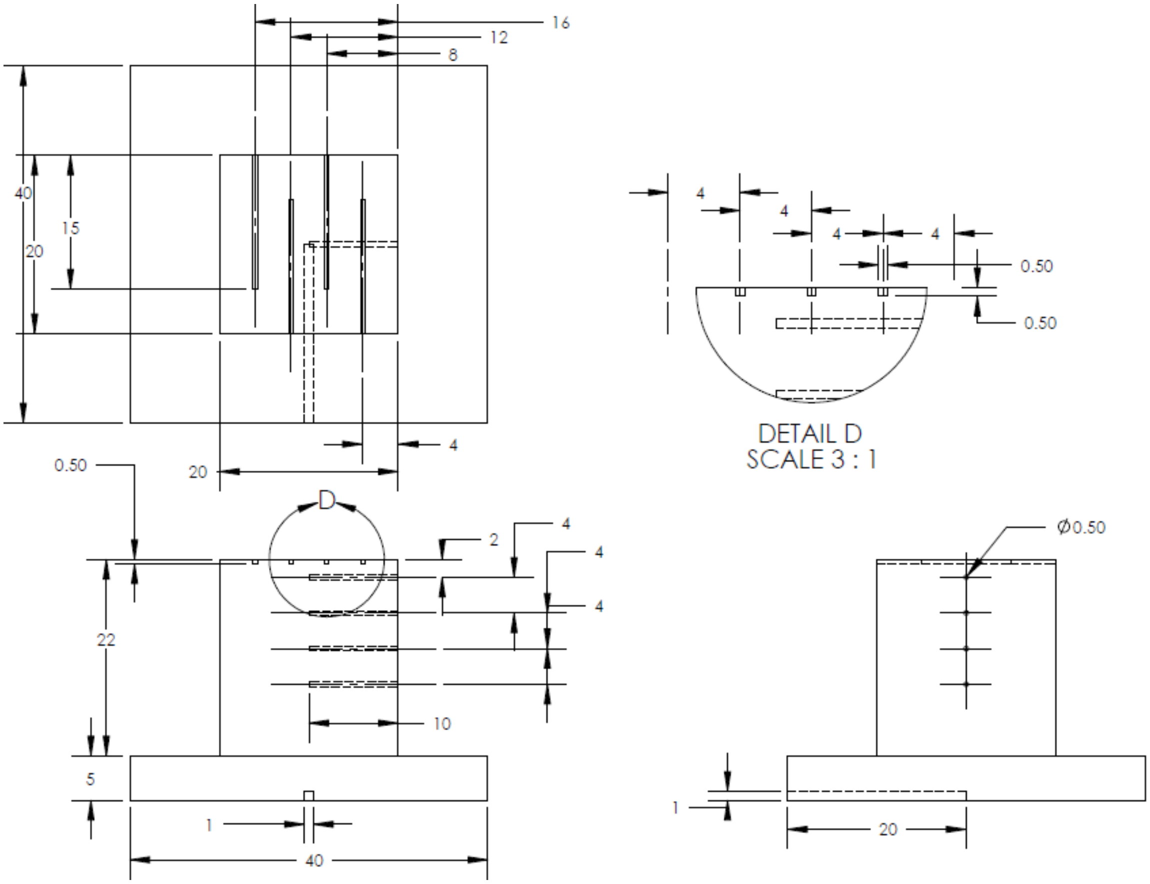

Figure A 1 CAD drawing of the aluminum block (all measurements in mm).

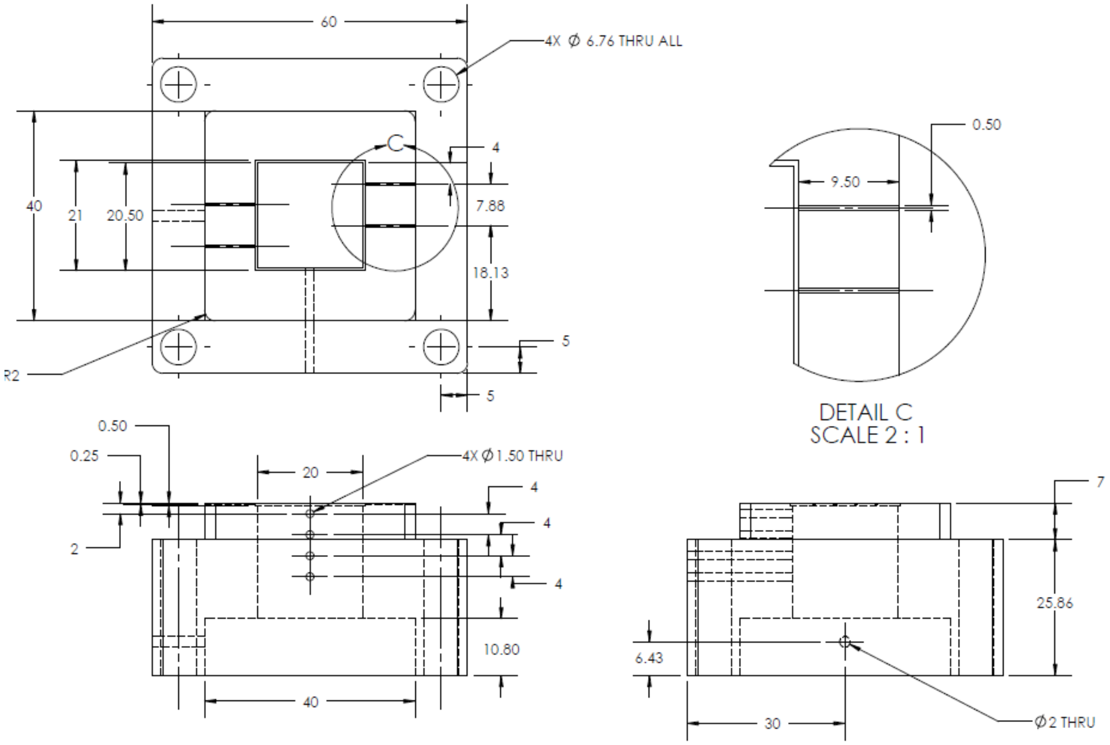

Figure A 2 CAD drawing of the insulation block (all measurements in mm).

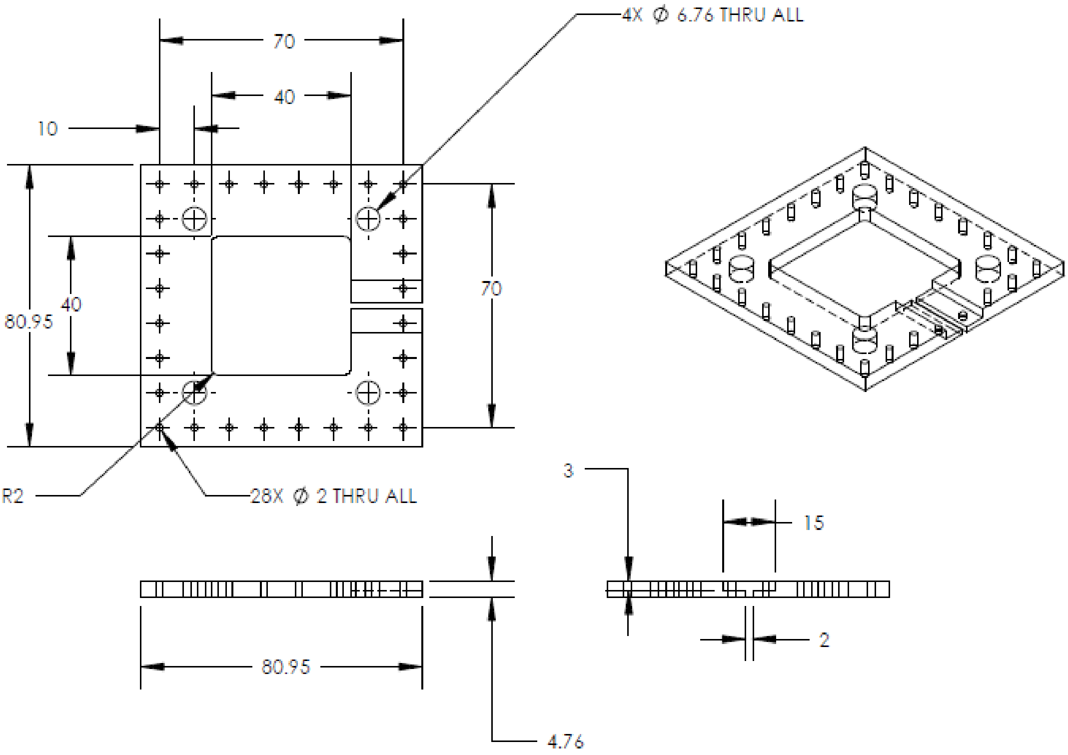

Figure A 3 CAD drawing of the perforated gas diffuser plate (all measurements in mm).

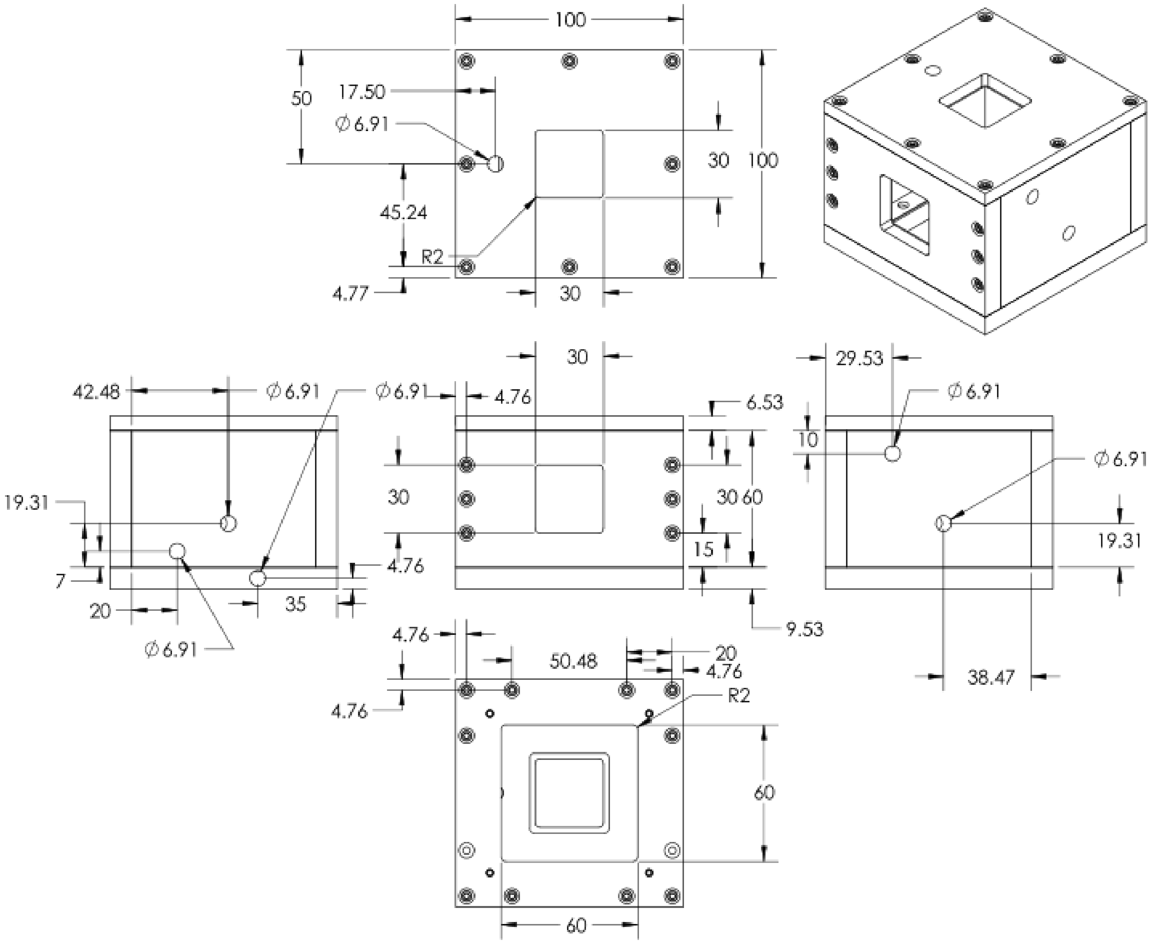

Figure A 4 CAD drawing of the acrylic chamber (all measurements in mm).

Appendix B Image Post Processing Scripts

In this section two MATLAB m-files are presented. The first, called "*AverageRaddii.m"*, extracts statistical information about the growth of multiple drops on a surface. The routine consists of the following series of steps. First, the contrast of the raw images is enhanced by using the *adapthisteq* function, followed by binary image segmentation with the *im2bw* function. Subsequently, the function *imfill* eliminates artificial light reflections that appear inside the droplets. Lastly, the Hugh transformation technique is applied using the *imfindcircles* function, which approximates the radius and the location of each drop assuming it is circular. In addition, the MATLAB script is capable of automatically estimating the number of droplets present on the surface; statistical information about the spatial distribution and size of the droplets can be obtained.

The second script, *"MultiDropTrack.m*", identifies and tracks single-droplet growth from sequence of images. The script reads a pair of subsequent images (i and $i+1$) and identifies a set of drops selected by the user in image i, and then relates the radius and the position of this drop with the closet drop in the following image $i+1$. The MATLAB code outputs the single-droplet growth evolution.

```
%=========================================================================
=========================================================================
=======================%
%%File Name: %AverageRaddii.m

close all
clear all
clc


k_i=3; % First image in the sequence
k_f=5; % Final sequence image in the sequence
k_pos=[k_i:1:k_f]; %Vector with all the images to process
dk=length(k_pos); % Range of images to be processed
int_con=0;
for k=1:dk
    k_val(k)=k_pos(k);
    ImgFile= sprintf('%d.jpg', k_pos(k))
    A_raw=imread(ImgFile); % Reads each image file and transform it
into a square matrix
    A=adapthisteq(A_raw);
    subplot(2, 3, 1);
    imshow(ImgFile);title('Image (2mmx2mm)(150x)');

    subplot(2, 3, 2);
    imshow(ImgFile);title('Image (2mmx2mm)(150x)');



    %Image segmentation in a binary image
    normalizedThresholdValue = 0.25; % In range 0 to 1.
    thresholdValue = normalizedThresholdValue * max(max(A)); % Gray
Levels.
    binaryImage = im2bw(A, normalizedThresholdValue); % bunary 1 (white)
0 (black)

    %invert the binary image
    binaryImage = imcomplement(binaryImage);

    %eliminating light reflection inside the droplets%
    % hole is an area of dark pixels surrounded by lighter pixels.
    binaryImage = imfill(binaryImage,'holes');

    %bwarea measures the area ocupy by the white circles
    AreaWhiteCircles=bwarea(binaryImage);
    % for 512*512 pixel images
    SurfCov(k,1)=AreaWhiteCircles/(512^2);  %Surface coverge for image
k
    time(k)=(k.*(1/2)); % [min]

    %Appliying Hough transformation to perfom edge recognition
    min_radii=2; %mininmun radius
    max_radii=180;%maximun radius
    [centers, radii, metric] = imfindcircles(binaryImage,[min_radii
max_radii],'Sensitivity',1.0,'EdgeThreshold',0.03);
```

```
    %% Selecting the circles that resembles the droplets present in the
surface

    a=metric;  % one-dimensional array
    b=abs(a);  % rectifying the data
    c=max(b);  % finding out the maximum value
    m=min(a);
    d=.30*c;    % finding the threshold value, 70 percent of the
maximum value
    p=1;

    for i=1:size(a,1) % size of the array
        if b(i)<=d
        p=i;
           break
        end
    end

    NumStrong=p; %Number of droplets present in the surface
    NumStrong_k(k)=p;

    centersStrong = centers(1:NumStrong,:);%[pixels]
    radiiStrong = radii(1:NumStrong); %[pixels]
    metricStrong = metric(1:NumStrong);
    label=(1:NumStrong)';
    viscircles(centersStrong, radiiStrong,'EdgeColor','b'); %ploting
circles in the image


    subplot(2, 3, 3);
    imshow(binaryImage)
    title('Binary Image');axis square;

    fontSize = 7;   % Used to control size of "blob number" labels put
atop the image.
    labelShiftX = -8;   % Used to align the labels in the centers of
the coins.

    % Identifiying each droplet present in the imgae

for j = 1 : NumStrong         % Loop through all circles.
    text(centersStrong(j,1)+ labelShiftX, centersStrong(j,2),
num2str(j), 'FontSize', fontSize, 'FontWeight', 'Bold','Color','b');
end


%relation pixel to mm depending on the magnification 150x
```

```
pixsize=3.91546159;
radiiStrong=pixsize*radiiStrong; %[um]
radii_ave(k,1)=mean(radiiStrong); %[um]
subplot(2, 3, 4);
xvalues = [10:1:300];
hist(radiiStrong,xvalues);
axis([0 300 0 70])
h = findobj(gca,'Type','patch');
set(h,'FaceColor',[0 .5 0],'EdgeColor','b')
title('Droplet Radius Histogram');axis square;
xlabel('Raidus [um]');
ylabel('Number of Drops');
% Volume of each droplet
theta=120*pi/180;
V=(pi/24)*(radiiStrong.*10^-6).^3 .*((2-
3.*cos(theta)+(cos(theta)).^3)./(sin(theta).^3)).*10^6;% ml
V_total(k)=sum(V);

 radii_conca=vertcat(int_con,radiiStrong);
 int_con=radii_conca;

subplot(2, 3, 5);
plot(time,SurfCov, '-bo');
axis([0 100 0 0.7])
title('Surface Coverage');axis square;
xlabel('Time [min]');
ylabel('\epsilon');

 subplot(2, 3, 6);
 plot(time,radii_ave,'-bo');
 axis([0 100 0 180])
 title('<R> vs time');axis square;
 xlabel('Time [min]');
 ylabel('<R> [um]');

 %concatenates the radius and make an histogram of it

 Img_File_Out= sprintf('70RH-Output-%d',k_pos(k));
 saveas(gcf, Img_File_Out, 'bmp');


 %%%Saving the resutls in an Excel document
    % array results
 results= [0,0,0,0,0;label,centersStrong,radiiStrong, metricStrong];
 ExcFileName='testdata.xlsx';
 filename = ExcFileName;
 sheet=k;
 xlswrite(filename,results,sheet)

 filename = ExcFileName;
C = {'Label','Xc','Yc','Radii','Metric'};
sheet=k;
xlswrite(filename,C)
```

```
end

d_radii_ave=diff(radii_ave)./2.5;

xvalues = [10:1:300];
[N_drop,center_bin]=hist(radii_conca,xvalues);
figure, loglog(center_bin',N_drop','bo') ;


log_time=log10(time.*60)'; %log time in seconds
log_drop_area=log10( NumStrong_k./0.040189)'; %log drop density
figure, plot(log_time,log_drop_area,'bo');
title('Drop density');axis square;
xlabel('log(Time, sec)');
ylabel('log[Drop/cm^2]');




V_total=V_total'
figure, plot(log10(time'),log10(V_total),'bo');
title('Volume of water in surface');axis square;
xlabel('Time[s]');
ylabel('Volume[mL]');

%==================================================================
==================================================================
======================%
```

```
%======================================================================
========================================================================
======================%
%%File Name: %MultiDropTrack.m


%% This scrip is capable of traking the growht of multiple droplets
from an initial user selection %%%%%%%
% The translation between the pixel image to mm is done by pixsize
variable

close all
clear all
clc

%defiing the range of files to process
k_i=112; % First image in the sequence
k_f=200;  % Final sequence image in the sequence
k_pos=[k_i:1:k_f]; %Vector with all the images to process
dk=length(k_pos); % Range of images to be processed
int_con=0;
DropSel=[10 7   15  17 13   29  23  12]; % Set of droplets to track in
ki
DropSel_surr=[];

for k=1:dk-1
    k_val(k)=k_pos(k);
    %reading a the pair of images (image 1) and (image 2)
    ImgFile= sprintf('%d.jpg', k_pos(k))
    ImgFile_2= sprintf('%d.jpg', k_pos(k+1))

    A=imread(ImgFile); % Image i
    A_2=imread(ImgFile_2); % Image i+1


    subplot(2, 2, 1);
    imshow(ImgFile);title('Image (2mmx2mm)(150x)');axis square;



    % Threshold the image to get a binary image (only 0's and 1's) of
class "logical."
    % Method #1: using im2bw()
    normalizedThresholdValue = 0.3; % In range 0 to 1.
    thresholdValue = normalizedThresholdValue * max(max(A)); % Gray
Levels.
    binaryImage = im2bw(A, normalizedThresholdValue);
    binaryImage_2 = im2bw(A_2, normalizedThresholdValue);

    %eliminating light reflection inside the droplets,
    %black becomes white and white becomes black.
     binaryImage = imcomplement(binaryImage);
     binaryImage_2 = imcomplement(binaryImage_2);
```

```
    % Do a "hole fill" to get rid of any background pixels inside the
blobs.
    % hole is an area of dark pixels surrounded by lighter pixels.
    binaryImage = imfill(binaryImage,'holes');
    binaryImage_2 = imfill(binaryImage_2,'holes');



    %Detecting circles in image 1 and image 2
    min_radii=2;
    max_radii=180;
    [centers, radii, metric] = imfindcircles(binaryImage,[min_radii
max_radii],'Sensitivity',1.0,'EdgeThreshold',0.03);
    [centers_2, radii_2, metric_2] =
imfindcircles(binaryImage_2,[min_radii
max_radii],'Sensitivity',1.0,'EdgeThreshold',0.03);

    %%%Selecting the appropiated number of circles that resembles the
droplets%%%%
    % for image 1
    a=metric;
    b=abs(a);  % rectifying the data
    c=max(b);  % finding out the maximum value
    m=min(a);
    d=.30*c;    % finding the threshold value, say 70 percent of the
maximum value
    p=1;

    for i=1:size(a,1) % size of the array
        if b(i)<=d
        p=i;
           break
        end
    end

    % for image 2
    a_2=metric_2;
    b_2=abs(a_2);  % rectifying the data
    c_2=max(b_2);  % finding out the maximum value
    m_2=min(a_2);
    d_2=.30*c_2;    % finding the threshold value, say 70 percent of
the maximum value
    p_2=1;

    for i=1:size(a_2,1) % size of the array
        if b_2(i)<=d_2
        p_2=i;
           break
        end
    end



    NumStrong=p; %number of droplest in Image 1
```

```
    NumStrong_k(k)=p;



    NumStrong_2=p_2; %number of droplest in Image 1
    NumStrong_k_2(k)=p_2;

    %Ploting image 1 in a vector window, Image 1 in the first element
of
    %the window
    subplot(2, 2, 2);
    imshow(binaryImage)
    title('Numbered droplets');axis square;

    %Croping the vectors that contain the properties of the droplet to
the
    %NumStrong elements
    centersStrong = centers(1:NumStrong,:);
    radiiStrong = radii(1:NumStrong);
    metricStrong = metric(1:NumStrong);
    label=(1:NumStrong)';
    viscircles(centersStrong, radiiStrong,'EdgeColor','b');
    %Pixel size calibration
    pixsize=3.91546159;
    radiiStrong=pixsize*radiiStrong;
    radii_ave(k,1)=mean(radiiStrong); %[units:um]

    %for image 2
    centersStrong_2 = centers_2(1:NumStrong_2,:);
    radiiStrong_2 = radii_2(1:NumStrong_2);
    metricStrong_2 = metric_2(1:NumStrong_2);
    label_2=(1:NumStrong_2)';

    radiiStrong_2=pixsize*radiiStrong_2;
    radii_ave_2(k,1)=mean(radiiStrong_2); %[units:um]

    time(k)=(k.*(1/2)); %[min]

    %%% Ploting all the recognized circles in the binary image%%%%%%
    fontSize = 7;   % Used to control size of "blob number" labels put
atop the image.
    labelShiftX = -8;   % Used to align the labels in the centers of
the coins.

%     Loopp over all blobs printing their measurements to the command
window.

    for j = 1 : NumStrong         % Loop through all circles.
        text(centersStrong(j,1)+ labelShiftX, centersStrong(j,2),
num2str(j), 'FontSize', fontSize, 'FontWeight', 'Bold','Color','b');
    end
```

```
 %%%% Surrounding droplet for the first image %%%%%%%%%%

    for m=1:NumStrong
        d(m,1)=sqrt((centersStrong(DropSel(k),1)-centersStrong
(m,1)).^2+(centersStrong(DropSel(k),2)-centersStrong (m,2)).^2);
        d(m,2)=m;
    end

    [d_sort,index] = sort(d(:,1));

    %defining the radius of serch

    R_i= radiiStrong(DropSel(k),1);
    R_search = 2*R_i;

    %select the droplets which distance from central droplet is less
than
    %radius search
    for h=1:NumStrong
       if d_sort(h,1)< R_search
          d_closest(h)=d_sort(h,1);
       else
           d_closest(h)=0;
        end
    end

    d_close_clean=[d_closest(1:find(d_closest~=0,1))
d_closest(d_closest~=0)];
    DropSel_surr=index(1:length(d_close_clean))

     DropSel_surr_k{k,:}=DropSel_surr;
     Num_cell_DropSel_surr_k(k,:)=DropSel_surr_k(k,:);
     Num_vec_DropSel_surr_k= cell2mat(Num_cell_DropSel_surr_k(k)); %
Selection oif the droplets for the first image

    %%% Ploting  droplets in second element of the window%%%

    subplot(1, 2, 2);
    imshow(binaryImage)
    title('Binary Image');axis square;

    %color for the central droplet
    text(centersStrong(DropSel(k),1)+ labelShiftX,
centersStrong(DropSel(k),2), num2str(DropSel(k)), 'FontSize', fontSize,
'FontWeight', 'Bold','Color','r');

    %tag for the surrounding droplets
        for j = 2 : length(d_close_clean)
            pos=index(j);
            text(centersStrong(pos,1)+ labelShiftX,
centersStrong(pos,2), num2str(pos), 'FontSize', fontSize, 'FontWeight',
'Bold','Color','b');
```

```
        end



%%%%%%%%% tracking of the droplets%%%%%%%%%%%%%%%%%%%%%%%%%%%
theta=120*pi/180;
Radi_sel(k,:)=radiiStrong(DropSel(k,:));

for j=1 : length(DropSel(1,:))
   position of the droplets in the first image
   x_search(k,j)=centersStrong(DropSel(k,j),1);
   y_search(k,j)=centersStrong(DropSel(k,j),2);


   closest distance of all the droplets in the second image to the
first
             for h=1:NumStrong_2
                 dis_prev(h)=sqrt((x_search(k,j)-
centersStrong_2(h,1)).^2+(y_search(k,j)-centersStrong_2(h,2)).^2);
             end
             [~, DropSel_2] = min(dis_prev) %droplet value in the
second image

             DropSel(k+1,j)=DropSel_2;
             Radi_sel(k,j)= radiiStrong(DropSel(k,j))
             Single drop Volume
             V(k,j)=(pi/24)*(Radi_sel(k,j).*10^-6).^3 .*((2-
3.*cos(theta)+(cos(theta)).^3)./(sin(theta).^3)).*10^6;% ml

end

        %%% ploting multple droplets
        subplot(2, 2, 3);
        imshow(binaryImage)
        title('Binary Image');axis square;
        title('Selected droplets');axis square;



        for j = 1 : length(DropSel(k,:))
            pos=DropSel(k,j);
            text(centersStrong(pos,1)+ labelShiftX,
centersStrong(pos,2), num2str(pos), 'FontSize', fontSize, 'FontWeight',
'Bold','Color','r');

        end




       subplot(2, 2, 4);
```

```
       plot(Radi_sel,'o-')
       axis([4 250 0 250])
       title('Radius Evolution');axis square;
       xlabel('t[min]');
       ylabel('R[\mum]');


       subplot(2, 3, 5);
       loglog(Radi_sel,'o-')

       %position of the surronding droplets in the second image
              for y=1:length(DropSel_surr)
                   x_search_surr(y)=centersStrong(DropSel_surr(y),1);
                   y_search_surr(y)=centersStrong(DropSel_surr(y),2);
          end
       %search for the closest x_coordiante
       search_x_vec_surr{y,:}=
abs(bsxfun(@minus,centersStrong(:,1),x_search_surr(y)));
       Num_cell_search_x_vec_surr(y,:)=search_x_vec_surr(y,:);
       Num_vec_search_x_vec_surr =
cell2mat(Num_cell_search_x_vec_surr(y));
       [~,idx_x_surr(y)] =
min( Num_vec_search_x_vec_surr(:,1:size(Num_vec_search_x_vec_surr,2)));
       y_comp_surr(y)=centersStrong(idx_x_surr(y),2);

       %search for the closest y_coordiante
       search_y_vec_surr{y,:}=
abs(bsxfun(@minus,centersStrong(:,1),y_search_surr(y)));
       Num_cell_search_y_vec_surr(y,:)=search_y_vec_surr(y,:);
       Num_vec_search_y_vec_surr =
cell2mat(Num_cell_search_y_vec_surr(y));
       [~,idx_y_surr(y)] =
min( Num_vec_search_y_vec_surr(:,1:size(Num_vec_search_y_vec_surr,2)));
       x_comp_surr(y)=centersStrong(idx_y_surr(y),1);


        if y_search_surr(y)-0.5<y_comp_surr(y) & y_comp_surr(y)
<y_search_surr+0.5
           DropSel_surr(y)=idx_x_surr(y);
           elseif  x_search_surr(y)-0.5 < x_comp_surr(y) &
x_comp_surr(y) <x_search_surr(y)+0.5
               DropSel_surr(y)=idx_y_surr(y);
           else
           %closest distance of all the droplets in the second image to
the first
                 for h=1:NumStrong_2
                     dis_prev_surr(y,h)=sqrt((x_search_surr(y)-
centersStrong_2(h,1)).^2+(y_search_surr(y)-centersStrong_2(h,2)).^2);
                 end
                 [~, DropSel_surr_2(y,:)] = min(dis_prev_surr(y,:));
                  end
          DropSel_surr_out{k,:}=DropSel_surr_2;
          Num_cell_DropSel_surr_out(k,:)=DropSel_surr_out(k,:);
```

```
          Num_vec_DropSel_surr_out=
cell2mat(Num_cell_DropSel_surr_out(k,:))

   end

   %%%% Identifiying surronding droplets in the second image %%%%%%%
   %DropSel have been updated with the central droplet in the second
image
       for m=1:NumStrong_2
        d_2(m,1)=sqrt((centersStrong_2(DropSel,1)-
centersStrong_2(m,1)).^2+(centersStrong_2(DropSel,2)-
centersStrong_2(m,2)).^2);
        d_2(m,2)=m;
       end

       [d_sort_2,index_2] = sort(d_2(:,1)); %Sorting decending the
distance from the central droplet

        R_surr_2= radiiStrong(DropSel,1); % updating the radii of
search with the new value of the Dropsel
        R_search_2 = 2*R_surr_2;

        %select the droplets which distance from central droplet is
less than
        %radius search
        for h=1:NumStrong_2
           if d_sort_2(h,1)< R_search_2
              d_closest_2(h)=d_sort_2(h,1);
           else
               d_closest_2(h)=0;
            end
        end

        %deleting all the zero values form the vector with the distance
of the
        %droplets closer to centrarl droplet
        d_close_clean_2=[d_closest_2(1:find(d_closest_2~=0,1))
d_closest_2(d_closest_2~=0)];

      DropSel_surr_2=index_2(1:length(d_close_clean_2));



        subplot(1, 2, 2);
        imshow(binaryImage)
        title('Binary Image');axis square;

        %color for the central droplet
        text(centersStrong(DropSel,1)+ labelShiftX,
centersStrong(DropSel,2), num2str(DropSel), 'FontSize', fontSize,
'FontWeight', 'Bold','Color','r');

        %tag for the surrounding droplets
        for j = 2 : length(d_close_clean)
```

```
            pos=index(j);
            text(centersStrong(pos,1)+ labelShiftX,
centersStrong(pos,2), num2str(pos), 'FontSize', fontSize, 'FontWeight',
'Bold','Color','b');

        end

pixsize=3.91546159;
radiiStrong=pixsize*radiiStrong;
radii_ave(k,1)=mean(radiiStrong); %[units:um]


subplot(2, 3, 4);
xvalues = [10:1:300];
hist(radiiStrong,xvalues);
axis([0 300 0 70])
h = findobj(gca,'Type','patch');
set(h,'FaceColor',[0 .5 0],'EdgeColor','b')
title('Droplet Radius Histogram');axis square;
xlabel('Raidus [um]');
ylabel('Number of Drops');





 radii_conca=vertcat(int_con,radiiStrong);
 int_con=radii_conca;

subplot(2, 3, 5);
plot(time,SurfCov, '-bo');
axis([0 100 0 0.7])
title('Surface Coverage');axis square;
xlabel('Time [min]');
ylabel('\epsilon');

 creating a ploting matrix for the first five elements





Radii_plot=radiiStrong(Num_vec_DropSel_surr_k(1:length(Num_vec_DropSel_
surr_k),1),1)


Radii_plot_cell{:,k}=radiiStrong(Num_vec_DropSel_surr_k(1:length(Num_ve
c_DropSel_surr_k),1),1)

 subplot(2, 2, 3);
 plot(time, Radii_plot,'-o'); hold on;
 axis([0 100 0 180])
 title('r vs time');axis square;
 xlabel('Time [min]');
```

```
 ylabel('r [um]');

 %concatenates the radius and make an histogram of it




 Img_File_Out= sprintf('45RH-Output-%d',k_pos(k+1));
 saveas(gcf, Img_File_Out, 'jpg');


 %%Saving the resutls in an Excel document
    array results
 results= [Radii_plot];
 ExcFileName='radii_surr.xlsx';
 filename = ExcFileName;
 sheet=k;
 xlswrite(filename,results,sheet)




 drawnow


end

d_radii_ave=diff(radii_ave)./2.5;

xvalues = [10:1:300];
[N_drop,center_bin]=hist(radii_conca,xvalues);
figure, loglog(center_bin',N_drop','bo') ;

log_time=log10(time.*60)'; %log time in seconds
log_drop_area=log10( NumStrong_k./0.040189)'; %log drop density
figure, plot(log_time,log_drop_area,'bo');
title('Drop density');axis square;
xlabel('log(Time, sec)');
ylabel('log[Drop/cm^2]');

% V_total=V_total'
figure, plot(log10(time'),log10(V_total),'bo');
title('Volume of water in surface');axis square;
xlabel('Time[s]');
ylabel('Volume[mL]');

size_V=size(V)
diff_time=time+0.25;

for j=1:size_V(1,2)
rate of volume growth at each droplet
    diff_vol(:,j)=diff(V(:,j)); % length(diff_vol)= length(V_total)-1
    diff_vol_smooth(:,j)= smooth(diff_vol(:,j),0.5);
```

```
end

length_plot_diff=size(diff_vol)


diff_time=diff_time(1:length_plot_diff(1))';
figure, plot(diff_time,diff_vol_smooth);
title('dv/dt vs t');axis square;
xlabel('Time[s]');
ylabel('dv/dt[mL/s]');

 %======================================================================
========================================================================
=======================%
```

Appendix C Effect of Surface Subcooling Temperature on Dropwise Condensation Dynamics

This section presents average radius growth dynamics for a set of dropwise condensation experiments on a Teflon-coated silicon surface. The experiments were performed at three different surface subcooling temperatures (ΔT_{Sub} = 15 °C, 10 °C, and 5 °C) for a constant relative humidity (RH = 70%). The experimental procedure is the same as for the condensation experiments described in CHAPTER 3. Figure C 1shows the dynamics of average droplet radius growth with time for the three different surface subcooling temperatures during regime (ii). A power-law fit to the data is shown for each sub-regime of growth with the transition times t_1 and t_2. Figure C 2 shows the dependence of the power-law exponents on surface subcooling temperature during regimes (ii_A) and (ii_B).

During regime (ii_A), the power-law exponent is increased at the largest surface subcooling temperature, and as a result, the time elapsed before the transition to regime (ii_B) is delayed. As previously discussed in Chapter 3, the growth of droplet average radius at early stages of growth (when the distribution of droplets size is narrow) is similar to single-droplet growth. Changes in the rate of growth behavior with surface subcooling are thus expected. Conversely, the exponent of the power law during regime (ii_B) is insensitive to surface subcooling as a result of the predominant influence of coalescence on the droplet growth.

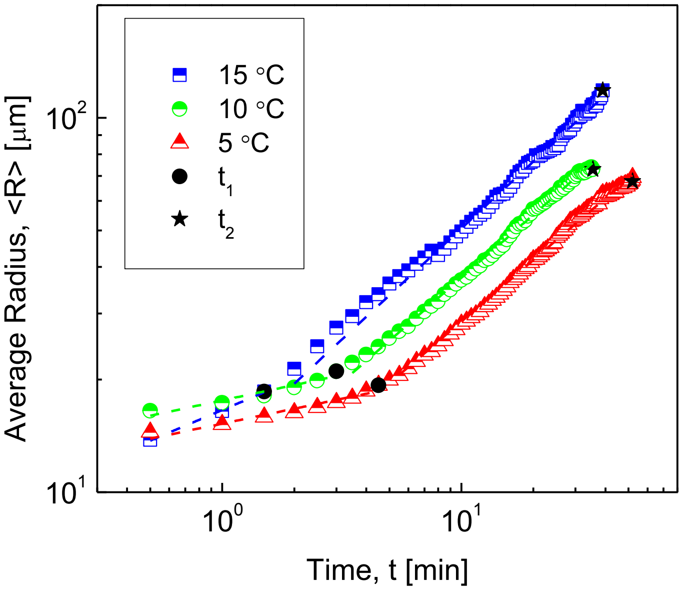

Figure C 1Average radius over time at RH = 70% for three surface subcooling temperatures of 5 ^{0}C, 10 ^{0}C, and 15 ^{0}C.

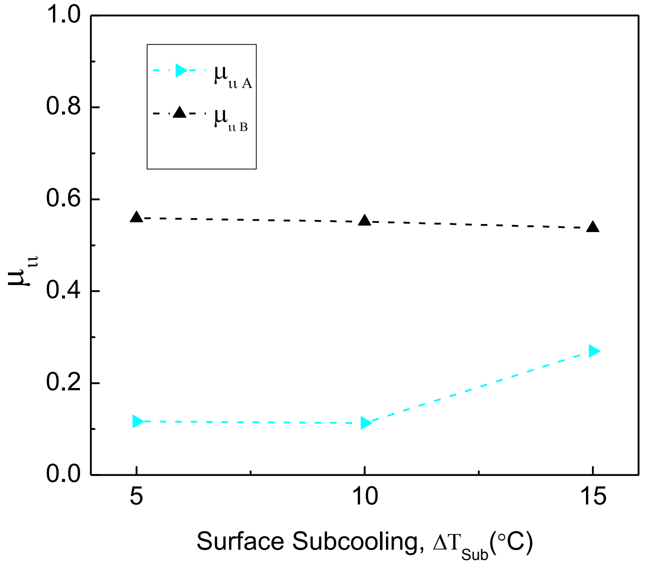

Figure C 2 Power-law exponent for a fit to the temporal average radius data of the form $<R>\sim t^{\mu}$ for regime (ii_A) (μ_{ii_A}) and regime (ii_B) (μ_{ii_B}) at three surface subcooling temperatures of 5 ^{0}C, 10 ^{0}C and 15 ^{0}C.

Appendix D Experiment Repeatability and Uncertainty Analysis for Measured Variables

This section discusses the repeatability of the results presented and the uncertainty in the measurements of temperature and relative humidity. An uncertainty analysis is provided for the calculated variables (error dispersion), such as the droplet rate of growth.

Figure D 1 shows experimental results of the average droplet radius growth for two different experiments carried out under the same experimental conditions (RH = 70 % and ΔT_{Sub} = 10 °C). There are negligible differences in the trends and the magnitudes observe during the two different experiments, providing confidence in the repeatability.

All of the T-type thermocouples were calibrated by using the set-up illustrated in Figure D 2. The calibration procedure consisted of measuring the temperature with an RTD sensor (PT100, Omega) at a controlled temperature routine in an oil thermal bath (Hart Scientific 7103 Micro-Bath, Fluke). The temperature measurements were referenced to a constant-temperature cell (TRCIII, Omega). A sixth-order polynomial relation was used to correlate the measured voltage difference for each thermocouple with the temperature of the bath measured by an RTD sensor, as illustrated in Figure D 3. The uncertainty of the temperature measurement was calculated by following standard uncertainty analysis [65] Including the errors induced from the DAQ system (34970A, Agilent) voltage reading (1 μV), the RTD temperature sensor (0.1 °C), the temperature control in the oil thermal bath (0.05 °C), and the constant-temperature cell (0.1 °C), there is ±0.3 °C uncertainty in the thermocouple temperature measurements.

The uncertainty associated with indirect measurement of droplet radius is computed by estimating the error induced during the spatial resolution calibration and the image post-processing algorithm (described in Appendix B). The main source of error in the droplet size measurement comes from the uncertainty in the distance between the lines on the calibration target grid (±0.5 µm). An image post-processing algorithm was developed in MATLAB to measure the size of the grid pattern. The sequence of images shown in Figure D 4 illustrates the calibration procedure. The algorithm uses a Hough Transform to detect the orientation of the lines in the grid. The algorithm then rotates the image and approximates the location of the intersections of the lines in the grid; the distance between the lines is computed in pixels with an error of ±0.25 µm. In conjunction with the error induced from the post-processing algorithm presented in Appendix B, the total uncertainty in the measurement of droplet radius is ± 0.6 µm/pixel.

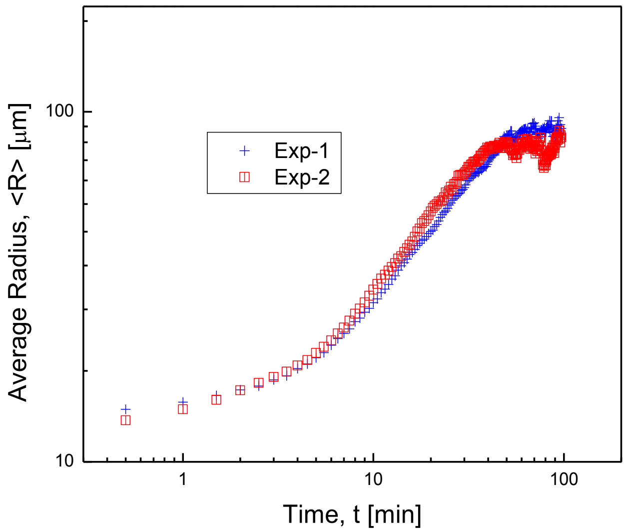

Figure D 1 Average radius versus time for two different experiments performed under the same experimental conditions ($RH = 70$ % and $\Delta T_{Sub} = 10$ °C).

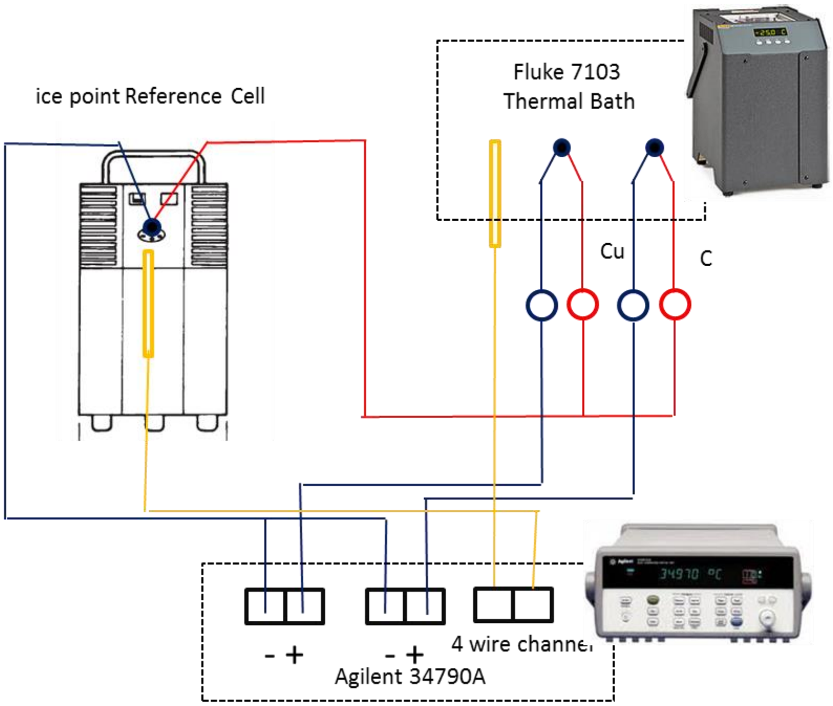

Figure D 2 Schematic diagram of the set-up used for thermocouple calibration.

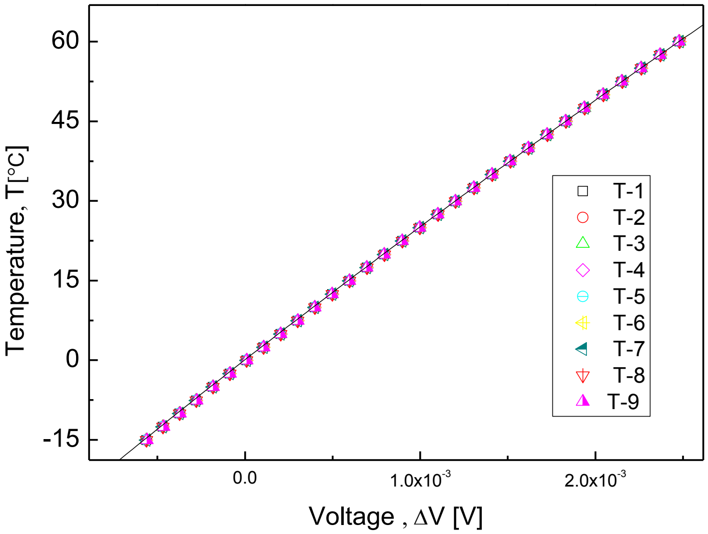

Figure D 3 Calibration curve for T-type thermocouples.

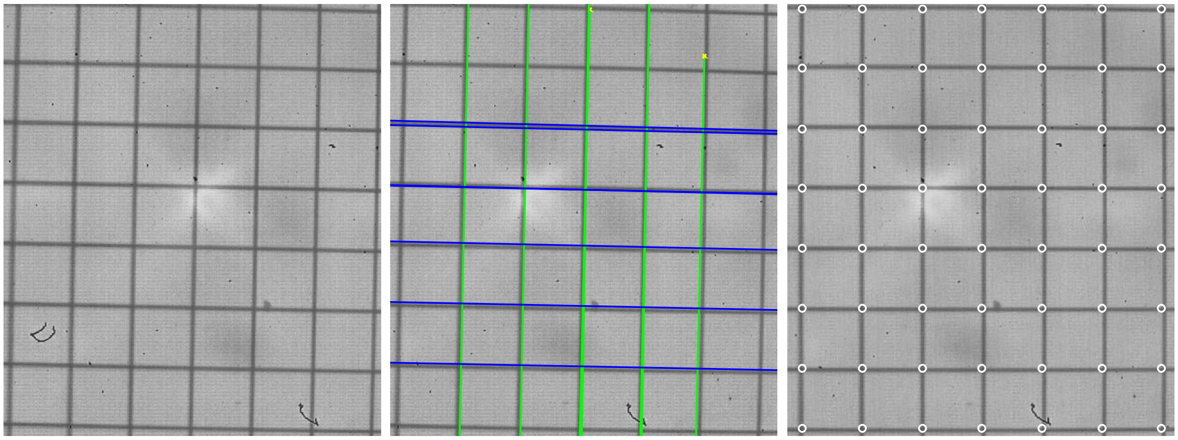

Figure D 4 Sequence of images showing the steps performed to measure the space between corners of the grid; used for image calibration.

Appendix E Considerations on Air Flow Velocity Inside Test Section

This section discusses possible effects of advective mass transport of vapor during the condensation experiment performed. Keeping small velocities in the air inside the test section is required to guarantee that water vapor is supplied to the condensing surface mainly due to diffusion. Special care was placed on designing a test section that reduces convective effects; 28 holes of 28 mm diameter each are located in the perforated plate shown in Figure A 3 in Appendix A that homogenously distribute the air flow inside the chamber.

Since the dynamics of the air flow inside the chamber is complicated, and the mass flow rate of vapor-air mixture that passes through the test section is continuously changing due to the controller actuation, a rough estimate of the velocity inside the test section can be obtained by assuming a constant volumetric flow into the chamber. This approximation is reasonable when the relative humidity inside the chamber is stable and close to the set point. By conservatively assuming 1 L/min is entering the chamber (the maximum possible flow rate allowed by the mass controllers), the maximum air velocity in the chamber occurs at the outlet from each hole in the perforated plate (0.49 mm/s). The actual velocity near the condensing surface is expected to be significantly lower than this value, but nonetheless, the contribution of advective transport is estimated form this velocity value. The Peclet number (Pe_L) for mass transport, given by $Pe_L = \mathrm{Re}_L\, Sc = LU / \mathrm{D}_{AB}$, where Re_L is the Reynolds number, Sc is the Schmidt number, L is the length scale (length of the sample), U is the velocity of the air, and D_{AB} is the diffusivity of water vapor in air at 20 °C (D_{AB} = 26 mm^2/s), compares the contribution of advective to diffusive mass transport. For the test chamber conditions, $Sc = 0.58$ and $Pe_L = 0.37$, which indicates that mass diffusion dominates over advective mass transport.

VITA

VITA

Julian E. Castillo grew up in Cali, Colombia. He received his Bachelor's degree in Mechanical Engineering in 2009 from Universidad del Valle, Colombia. His Bachelor's thesis was awarded the "Claudio Fernández Riva" prize, and was focused on the development of new polymer electrolyte membranes for fuel cell technologies. He is recipient of a Fulbright –COLCIENCIAS scholarship. He is currently a M.S. student at Purdue University working with Prof. Suresh V. Garimella and Prof. Justin A. Weibel. His Master's thesis research work studies droplet growth dynamics during dropwise condensation of humid air.